Cell

Topical therapy for regression and melanoma prevention of congenital giant nevi

Graphical abstract

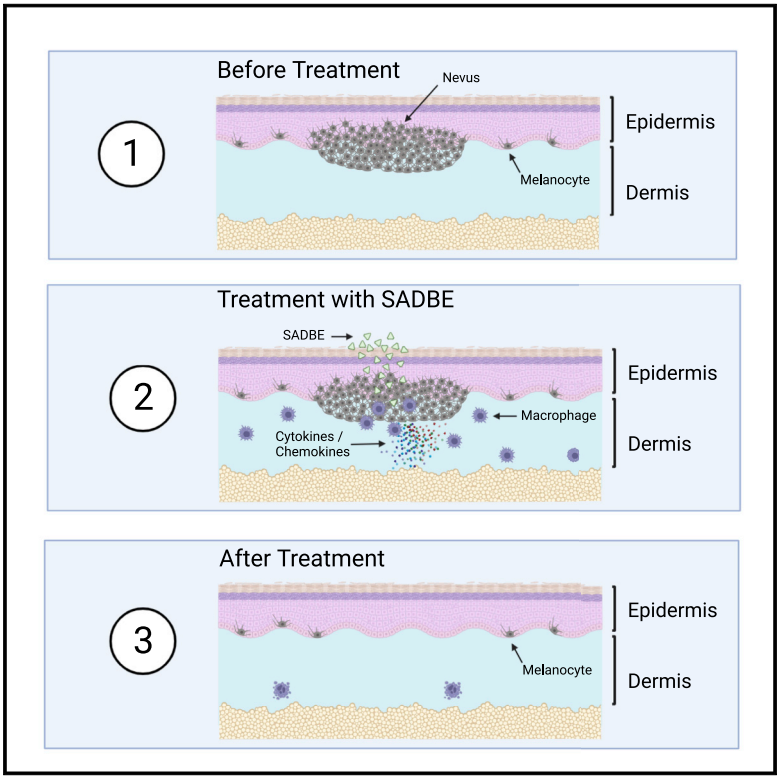

Highlights

- Models of melanocyte inducible *Nras*^{Q61R} mimic human congenital melanocytic nevi
- Locally delivered MEK, PI3K, and c-KIT inhibitors are able to regress the nevi
- SADBE regresses nevi in mice and human CMN xenografts and prevents melanoma in mice
- SADBE induces inflammation and recruits macrophages that lead to nevus clearance

Authors

Yeon Sook Choi, Tal H. Erlich, Max von Franque, ..., Shadmehr Demehri, Elena B. Hawryluk, David E. Fisher

Correspondence

dfisher3@mgh.harvard.edu

In brief

Large congenital nevi, or highly pigmented regions of skin, can present major cosmetic and psychosocial issues and have a significant chance of turning into malignant melanoma. However, current treatment methods provide only partial removal and can lead to scarring. Here, congenital nevus mouse models were developed and used to identify topical therapies that were highly effective at clearing nevi and protecting against melanoma formation.

Choi et al., 2022, Cell *185*, 2071–2085
June 9, 2022
https://doi.org/10.1016/j.cell.2022.04.025

CellPress

Cell

CellPress

Article

Topical therapy for regression and melanoma prevention of congenital giant nevi

Yeon Sook Choi,[1,2,12] Tal H. Erlich,[1,2,12] Max von Franque,[1,2,3] Inbal Rachmin,[1,2] Jessica L. Flesher,[1,2] Erik B. Schiferle,[1,2] Yi Zhang,[4] Marcello Pereira da Silva,[1,2] Alva Jiang,[4] Allison S. Dobry,[2] Mack Su,[1,2] Sharon Germana,[1,2] Sebastian Lacher,[1,2] Orly Freund,[1,2] Ezra Feder,[1] Jose L. Cortez,[5] Suyeon Ryu,[6] Tamar Babila Propp,[1,2] Yedidyah Leo Samuels,[1,2] Labib R. Zakka,[7] Marjan Azin,[1,2] Christin E. Burd,[8] Norman E. Sharpless,[9] X. Shirley Liu,[4] Clifford Meyer,[4] William Gerald Austen, Jr.,[10,11] Branko Bojovic,[9,10] Curtis L. Cetrulo, Jr.,[10,11] Martin C. Mihm,[7] Dave S. Hoon,[6] Shadmehr Demehri,[1,2] Elena B. Hawryluk,[2] and David E. Fisher[1,2,13,*]

[1]Cutaneous Biology Research Center, Department of Dermatology, Massachusetts General Hospital, Harvard Medical School, Charlestown, MA 02129, USA
[2]Department of Dermatology, Harvard Medical School, Massachusetts General Hospital, Boston, MA 02114, USA
[3]Massachusetts Institute of Technology, 77 Massachusetts Ave, Cambridge, MA 02139
[4]Department of Data Science, Dana Farber Cancer Institute, Harvard T.H. Chan School of Public Health, Boston, MA 02215
[5]Department of Dermatology, University of New Mexico, Albuquerque, NM 87106, USA
[6]Department of Translational Molecular Medicine, Saint John's Cancer Institute Providence Health and System, Santa Monica, CA 90404
[7]Department of Dermatology, Brigham and Women's Hospital, Harvard Medical School, Boston, MA 02115, USA
[8]Department of Cancer Biology and Genetics, The Ohio State University, Columbus, OH, USA
[9]National Cancer Institute, National Institute of Health, Bethesda, MD 20892
[10]Division of Plastic and Reconstructive Surgery, Massachusetts General Hospital, Harvard Medical School, Boston, MA 02114, USA
[11]Division of Plastic Surgery, Shriners Hospital for Children, Boston, Harvard Medical School, Boston, MA 02114, USA
[12]These authors contributed equally
[13]Lead contact
*Correspondence: dfisher3@mgh.harvard.edu
https://doi.org/10.1016/j.cell.2022.04.025

SUMMARY

Giant congenital melanocytic nevi are *NRAS*-driven proliferations that may cover up to 80% of the body surface. Their most dangerous consequence is progression to melanoma. This risk often triggers preemptive extensive surgical excisions in childhood, producing severe lifelong challenges. We have presented preclinical models, including multiple genetically engineered mice and xenografted human lesions, which enabled testing locally applied pharmacologic agents to avoid surgery. The murine models permitted the identification of proliferative versus senescent nevus phases and treatments targeting both. These nevi recapitulated the histologic and molecular features of human giant congenital nevi, including the risk of melanoma transformation. Cutaneously delivered MEK, PI3K, and c-KIT inhibitors or proinflammatory squaric acid dibutylester (SADBE) achieved major regressions. SADBE triggered innate immunity that ablated detectable nevocytes, fully prevented melanoma, and regressed human giant nevus xenografts. These findings reveal nevus mechanistic vulnerabilities and suggest opportunities for topical interventions that may alter the therapeutic options for children with congenital giant nevi.

INTRODUCTION

Congenital melanocytic nevi are benign proliferations of nevomelanocytes that are present at birth. Large or giant congenital nevi occur in approximately 1 in 20,000 births (Chien et al., 2010; Hashmi et al., 2009). The estimated rates of conversion from benign nevus to malignant melanoma are approximately 2% and 12% in patients with large and giant congenital nevi, respectively (Bett, 2005; Kinsler et al., 2009; Vourc'h-Jourdain et al., 2013; Zaal et al., 2005). Other side effects of congenital melanocytic nevi include weakened skin integrity within the lesions as well as major cosmetic and psychosocial ramifications due to their appearance (Koot et al., 2000; Price and Schaffer, 2010; Tromberg et al., 2005).

The current available treatments for patients with congenital melanocytic nevi include surgical excision, dermatome shaving, pigment-specific laser, and others (Ibrahimi et al., 2012; Viana et al., 2013). However, removal of a complete lesion by these approaches is often impossible. The development of alternative therapies that avoid the shortcomings of the current treatments

(such as extensive scarring) while minimizing the lifetime risk of melanoma is needed.

Activating *NRAS* mutations are the sole recurrent somatic mutation found in up to 80%–95% of large and giant congenital nevi (Bauer et al., 2007). The majority of *NRAS* mutations are Q61K or Q61R amino acid substitutions, resulting in a constitutively active NRAS protein (Bauer et al., 2007; Charbel et al., 2014; Kinsler et al., 2013). Shakhova and colleagues (Shakhova et al., 2012) demonstrated that transgenic mutant *Nras* targeting melanocytes via the tyrosinase promoter can cause Sox10-dependent giant congenital nevi in mice, in agreement with several groups who used *tyr::Nras* models to demonstrate and study nevi or progression to melanoma (Ackermann et al., 2005; Pawlikowski et al., 2015; Shakhova et al., 2012).

In this study, we describe the development and characterization of murine congenital nevus models that accurately recapitulate key features of human giant congenital nevi, including risk of progression to invasive melanoma. We utilized these preclinical models to test a collection of localized drug treatments and observed that MEK (mitogen-activated kinase)-targeted local therapies exhibit regressive activity. We additionally observed a profound clearance of the lesions following topical squaric acid dibutyl ester (SADBE)-based immunotherapy, an approach that also offered 100% protection against melanoma formation within treated skin of prospectively followed mice. The activity of SADBE was shown to be mediated by macrophages. Therefore, it was possible to confirm SADBE efficacy in xenografts of human resected giant nevi established in immunodeficient (SHO) mice that retain macrophage function. These data suggest that an immune-based approach that utilizes topical SADBE may hold therapeutic potential for human giant congenital nevi.

RESULTS

Melanocyte-specific *Nras*^{Q61R}-driven congenital nevus models recapitulate genetic and phenotypic features of human giant congenital nevi

We generated and then characterized both constitutive and inducible murine giant congenital nevus models and compared their features with those of corresponding human lesions. Melanocyte-specific *Nras*^{Q61R} mutant mice were generated by crossing lox-stop-lox (LSL)-*Nras*^{Q61R} knockin mice (Burd et al., 2014) with transgenic mice expressing homozygous Cre recombinase under the control of melanocyte-specific promoters, including *dopachrome tautomerase* (*Dct*) and *tyrosinase* (*Tyr*). Newborn mice harboring the *Dct*-Cre-mediated *Nras*^{Q61R} mutation displayed cutaneous hyperpigmentation and retained their congenital pigmented lesions throughout life, without spontaneous regression (Figures 1A and S1A). Abundant ectopic dermal melanin was detected in mutant skin (Figures 1B and S1B), and the melanin producing dermal melanocytes stained positively for the *Nras*^{Q61R} mutation (Figure S1C). Melanocytic markers, such as S100, SOX10, MITF (microphthalmia associated transcription factor), and phospho-ERK (extracellular signal-regulated kinase), were also present within dermal nevus cells (Figures 1C, 1D, and S1D–S1F). When lesions from *Nras* mutant mice were juxtaposed with human giant congenital nevi (e.g., Figures 1G and S2), multiple comparable histologic features were detected. Similar to the human giant congenital nevi, the mutant mouse nevi were adjacent to adnexal structures while sparing other structures, distributed within papillary and reticular dermis extending into superficial subcutaneous fat, and combined with variably pigmented spindle-shaped nevus cells. In addition, superficial aggregates of nevus cells formed nests and penetrated along collagen bundles parallel to the long axis of the epidermis.

In order to assess proliferative vs senescent phases of nevus development, melanocyte-specific expression of inducible *Nras*^{Q61R} mutation was activated by topical 4-hydroxytamoxifen (tamoxifen) treatment in neonatal offspring of LSL-*Nras*^{Q61R} knockin mice crossed with tamoxifen-inducible *Tyr*-CreER^{T2} mice. 2 weeks after induction, skin hyperpigmentation was observed, driven by ectopic dermal melanocytes that developed in tamoxifen-treated areas of skin (Figures 1E, 1F, S1G, and S1H). We also generated mice by using constitutive *Tyr*-Cre-mediated *Nras*^{Q61R} expression. The combination of these alleles was lethal in most offspring. In addition to skin hyperpigmentation, the few surviving *Tyr*-Cre *Nras*^{Q61R} mutants displayed hydrocephalus (Figure S1I) and other neurologic abnormalities, such as neurocutaneous melanosis, (Figures S1J–S1N) which are in line with similar murine and human *Nras* mutations expressed in mice and in children (Kinsler et al., 2013; Pedersen et al., 2013; Shah, 2010; Shakhova et al., 2012).

Nras^{Q61R} mutation-driven congenital nevi exhibit proliferative and senescent phases

Since the therapeutic efficacies of various treatments may depend on whether nevus cells are proliferating or arrested/senescent, we quantified the proportion of dermal melanocytic cells in *Dct*-Cre *Nras*^{Q61R} mice, at various time points relative to date of birth, measuring proliferative and senescence markers. The results indicated that neonatal nevus cells are negative for p16^{Ink4a} (Figure 2A) and positive for Ki67 (Figure 2B), consistent with a proliferative phase. In contrast, adult nevus cells are positive for p16^{Ink4a} (Figure 2C), but not Ki67 (Figure 2D), consistent with growth arrest and senescence (Gray-Schopfer et al., 2006; Tran et al., 2012). Quantification of these data revealed that *Nras*^{Q61R} mutation-driven congenital nevi are initially proliferative and become senescent over approximately 3 weeks (Figure 2E, note left and right y axes), a feature that has also been observed in humans (Gerami and Paller, 2013; Leech et al., 2004; Phadke et al., 2011).

Nras^{Q61R}- driven nevi transform into invasive melanoma

Human giant congenital nevi carry a significant risk of melanomagenesis (Bajaj et al., 2009; Krengel et al., 2006; Shah, 2010). We, therefore, assessed the risk of melanoma development in our *Nras*^{Q61R} mutation-driven murine nevus models. Tumor-free survival curves for *Nras* mutant animals displayed significant rates of melanoma formation in *Dct*-Cre *Nras*^{Q61R} mice (Figure 3A) and *Tyr*-CreER^{T2} *Nras*^{Q61R} mice (Figure 3B) compared with control mice. In humans, melanomas derived from giant congenital nevi are typically heterozygous for mutant *NRAS* (Kinsler et al., 2013; Price, 2016). Consistent with this, we observed significant latency and sporadic frequency of

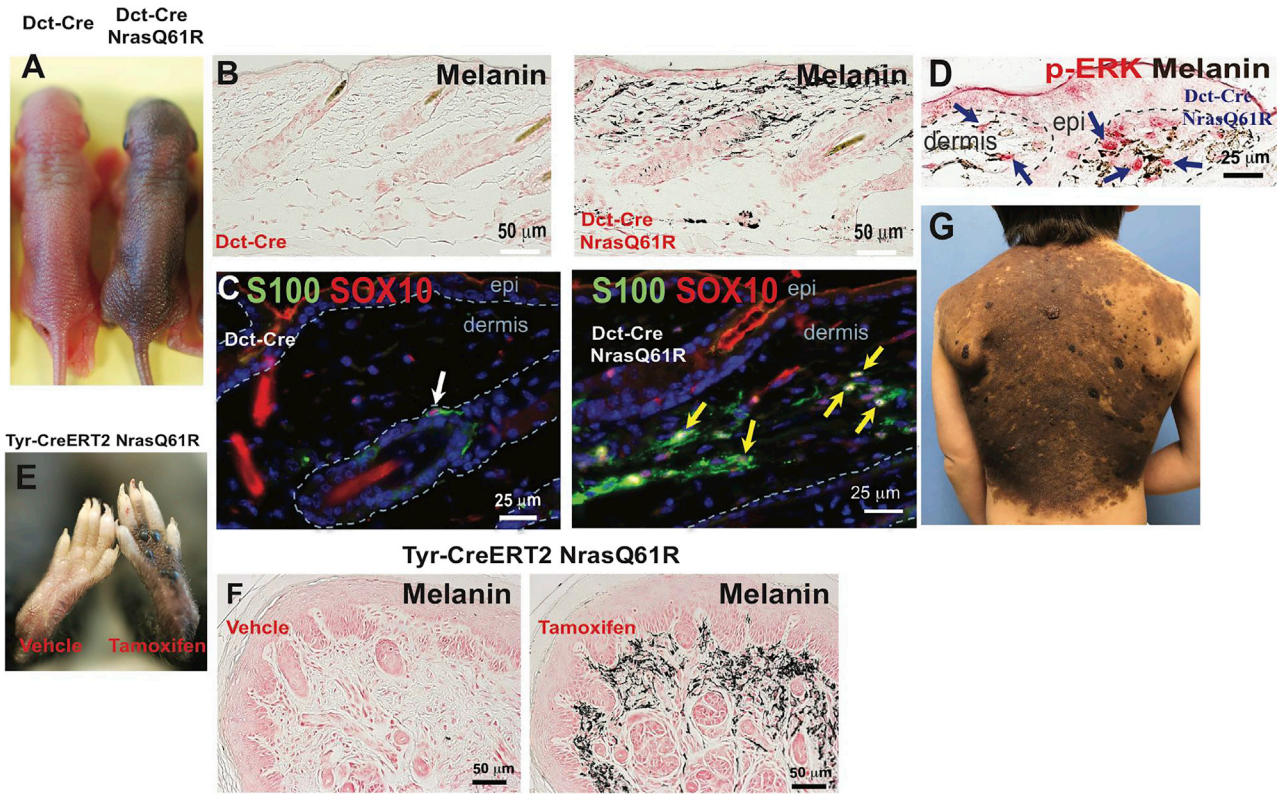

Figure 1. Melanocyte-specific *Nras*^{Q61R} mutant mice recapitulate histologic and molecular features of human giant congenital melanocytic nevi

(A) Features of melanocytic nevi in 3-day-old *Dct*-Cre *Nras*^{Q61R}.

(B) Melanin of adult *Dct*-Cre *Nras*^{Q61R} mice was detected by Fontana-Masson staining.

(C and D) Immunostains. Paraffin sections were immunostained for S100 (C, green), SOX10 (C, red), or p-ERK (D, red).

(E) Features of melanocytic nevi in tamoxifen-induced *Tyr*-CreER^{T2} *Nras*^{Q61R} mice.

(F) Melanin in tamoxifen-induced *Tyr*-CreER^{T2} *Nras*^{Q61R} mice was detected by Fontana-Masson staining.

(G) The clinical appearance of a human giant congenital nevus.

White arrow in (C) indicates normal signal in hair follicle. Yellow arrows in (C) indicate ectopic signals in the dermis of nevus skin. Blue arrows in (D) indicate positive signals.

See also Figures S1 and S2.

spontaneous melanoma formation in *Nras*$^{Q61R/+}$ heterozygous mice activated by either constitutive (*Dct*-Cre) or inducible (*Tyr*-CreER^{T2}) Cre alleles (Figures 3A and 3B, red lines), thus resembling another feature of human giant congenital nevi. Two copies of *Nras*^{Q61R} produced melanoma transformation with a shorter latency and a higher penetrance in both the constitutive (*Dct*-Cre) and inducible (*Tyr-CreER*^{T2}) backgrounds (Figures 3A and 3B, green lines). Furthermore, we found that *Dct*-Cre *Nras*^{Q61R} mutation-driven melanomas were positive for melanocytic markers, including S100, SOX10 (Figure 3C), and MITF (Figure 3H), and were highly proliferative (Figure 3D). The activating *Nras*^{Q61R} epitope was found in both models (Figures 3E and 3I), and 3 of 3 melanomas arising on heterozygous *Nras*^{Q61R} mice retained the wild-type *Nras* allele (Figure S3). The activation of MEK/ERK signaling in *Dct*-Cre *Nras*^{Q61R} nevus-derived melanomas was confirmed by immunofluorescence (Figures 3F and 3G). *Dct*-Cre *Nras*^{Q61R} mutation-driven murine melanomas (Figures 3L–3N) also showed similar histologic features when compared with those of human melanomas (Figures 3J and 3K).

RNA sequencing (RNA-seq) was performed on nevi containing pinna and tumors from *Dct*-Cre *Nras*$^{Q61R/+}$ and *Tyr*-CreER^{T2} *Nras*$^{Q61R/Q61R}$ mice and compared with normal pinna. Pigmentation/melanocytic genes were somewhat upregulated with larger upregulation in homozygous *Nras*$^{Q61R/Q61R}$ nevi (Figure S4A), likely reflecting the relative mixture of nevus cells within other skin cells. Previously published human CMN (congenital melanocytic naevus) expression data (Martins da Silva et al., 2019) showed heterogeneous expression patterns with some showing only weak melanocytic genes (e.g., MITF, SOX10), whereas others showing higher melanocytic genes expression (Figure S4B). In addition, there is evidence of upregulated interferon-α response as well as G2M checkpoint in the mouse CMN models compared with normal skin (Figure S4C). Upregulated transcription factors, such as hematopoietic factor Gfi1b (fold change = 33.3, q value < 3.7×10^{-2}), regulatory

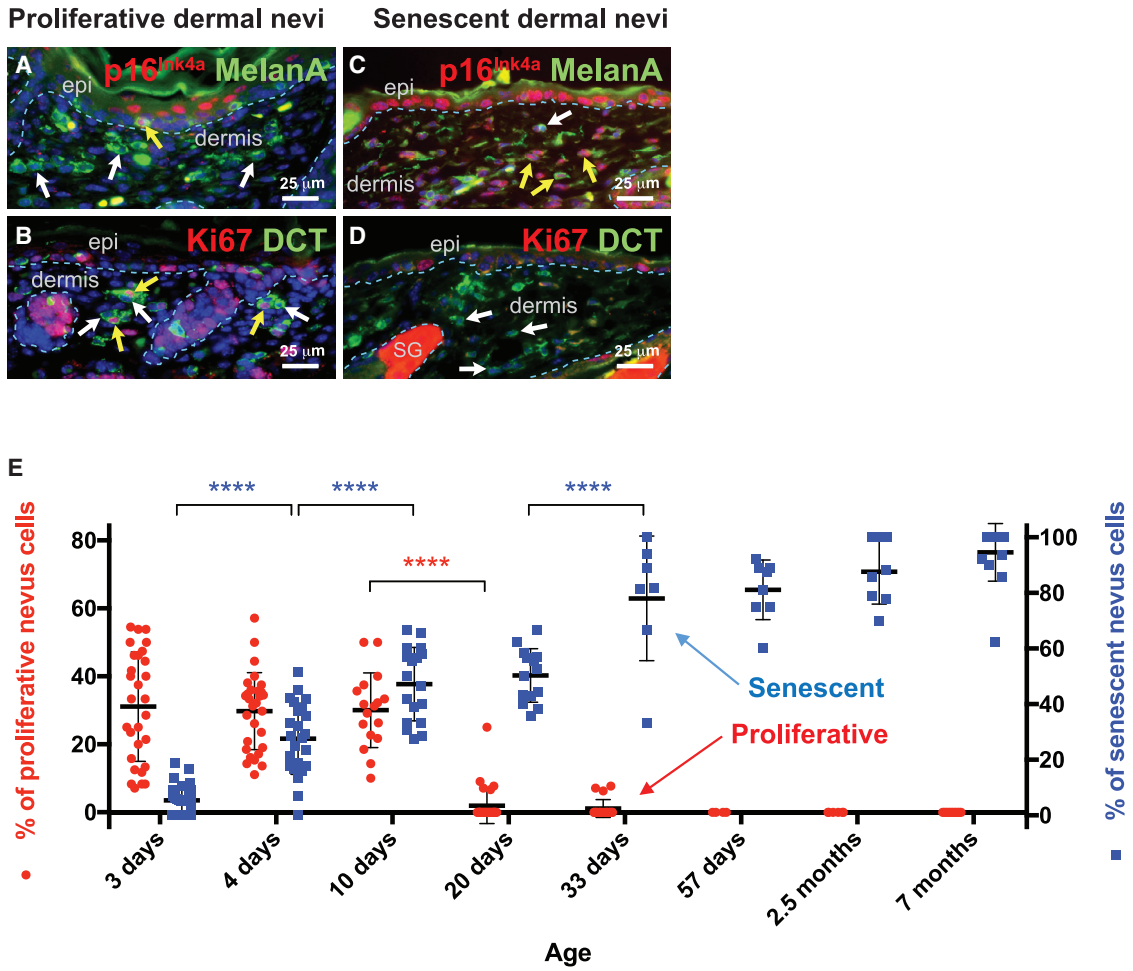

Figure 2. *Nras*^{Q61R} mutation-driven congenital nevi are initially proliferative and subsequently become senescent

(A–D) (A and B) Representative images of proliferative nevi. (C and D) Representative images of senescent nevi. Paraffin sections were immunostained for p16^{Ink4a} (A and C, red), MelanA/MART1 (A and C, green), Ki67 (B and D, red), or DCT (B and D, green). Yellow arrows indicate double-positive cells, and white arrows indicate single-positive cells.

(E) Dorsal skin samples from *Dct*-Cre *Nras*$^{Q61R/Q61R}$ mutant mice were harvested at the ages indicated. Samples from three mice of each age group, with five to ten of nonadjacent samples per mouse, were quantified. Nevus cell proliferation and senescence were measured by immunofluorescence staining for Ki67 and p16^{Ink4a}, respectively. Quantification of the above staining revealed a statistically significant decrease in proliferative nevus cell between 10 and 20 days of age (E, red). The percentage of senescent nevus cells gradually increases between age groups until mice reach approximately 1 month of age (E, blue). Red- and blue-colored dots indicate mean percentages of nevus cells that are proliferative (left y axis) or senescent (right y axis), respectively. The bars represent the standard error of the mean (SEM). p values were calculated using one-way ANOVA with Tukey's multiple comparison test (****p < 0.0001).

T cell-specific factor Foxp3 (fold change = 3.7, q value < × 1.5 10^{-2}), and lymphoid specific transcription factor Spi-b (fold change = 3.0, q value < 4.5 × 10^{-2}) also indicate immune infiltration in heterozygous nevi. Gfi and Foxp3 are included among the top 20 LISA (epigenetic Landscape *in silico* Sequence Analysis)-predicted TF (transcription factor) regulators of the differentially expressed genes, along with other immune-related factors, Stat1, Stat3, Runx1, Irf4, RelA, and Tbx21 (Figure S4D). In tumors, both models exhibited heterogeneity in expression patterns, likely reflecting variable second genetic events that followed the initiating *Nras*^{Q61R} genomic event. Ngfr and Sox10 were upregulated in *Dct*-Cre *Nras*$^{Q61R/+}$ tumors (Figure S4E). Interestingly, Sox9 was downregulated in tumors from both models, similar to SOX9 in human melanoma (Yang et al., 2019). The interferon-α response was upregulated in the mouse tumors (Figure S4F). Human CMN samples (Martins da Silva et al., 2019) expressed a number of pathways in common with the murine CMNs, including upregulated interferon-α and downregulated oxidative phosphorylation and adipogenesis (Figure S4G). We therefore utilized these murine models of *Nras*^{Q61R}-mutation-driven melanocytic nevi in subsequent experiments to preclinically evaluate therapeutic strategies to regress nevi and prevent progression to melanoma.

Signaling inhibitors can regress *Nras*^{Q61R} mutation-driven melanocytic nevi

We hypothesized that MAPK or PI3K pathway inhibitors (either alone or in combination) may lead to regression of *Nras*^{Q61R}

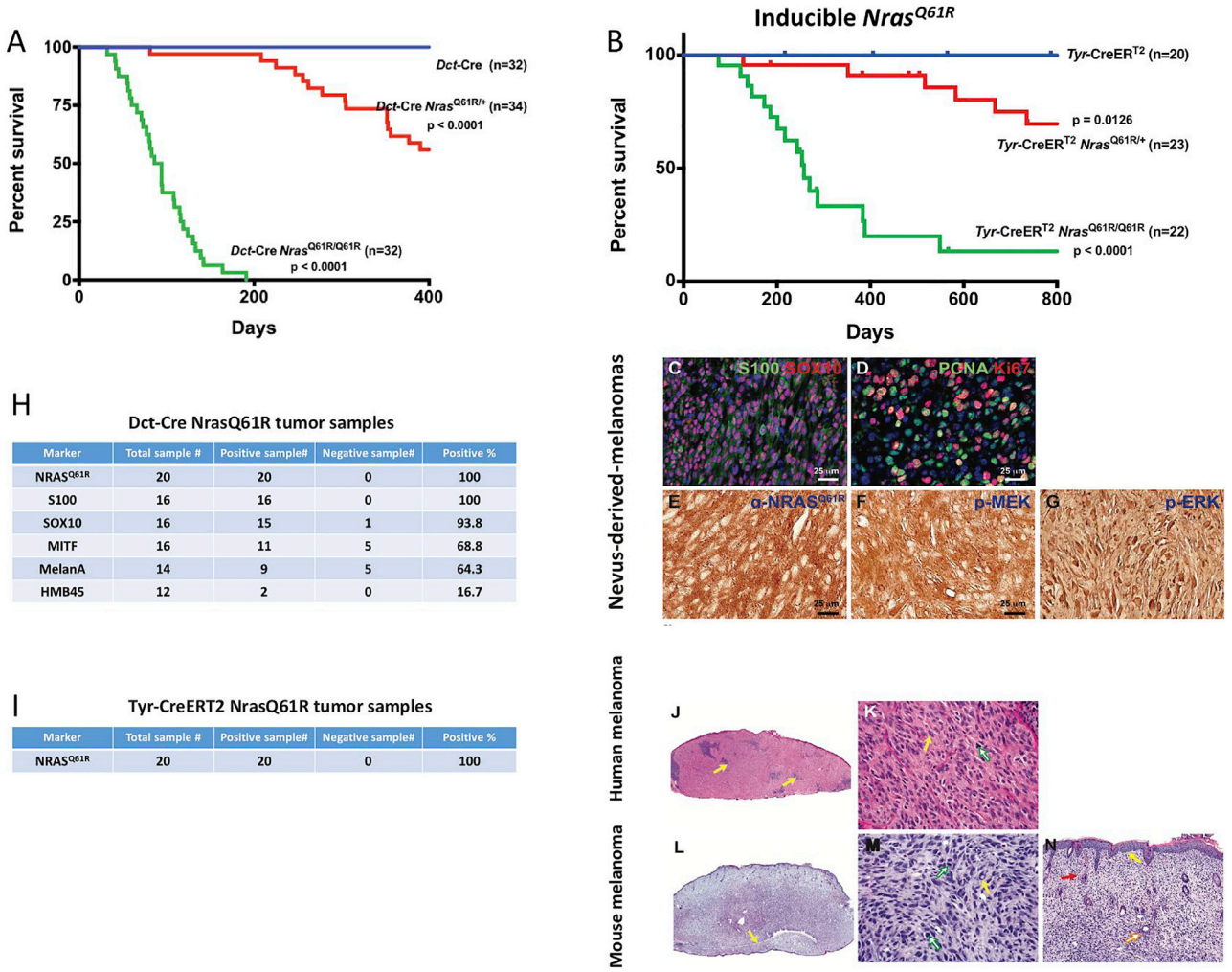

H

Dct-Cre NrasQ61R tumor samples

Marker	Total sample #	Positive sample#	Negative sample#	Positive %
NRAS^{Q61R}	20	20	0	100
S100	16	16	0	100
SOX10	16	15	1	93.8
MITF	16	11	5	68.8
MelanA	14	9	5	64.3
HMB45	12	2	0	16.7

I

Tyr-CreERT2 NrasQ61R tumor samples

Marker	Total sample #	Positive sample#	Negative sample#	Positive %
NRAS^{Q61R}	20	20	0	100

Figure 3. Melanocyte-specific *Nras*^{Q61R} activating mutation in mice results in high incidence of melanoma with shared histologic features of human melanoma

(A) *Dct*-Cre *Nras*$^{Q61R/Q61R}$ mutant (green, n = 35), *Dct*-Cre *Nras*$^{Q61R/+}$ mutant (red, n = 34), and *Dct*-Cre control (blue, n = 32) mice were examined to compare the incidence of *Nras*^{Q61R} mutation-driven melanoma formation. Survival curves were plotted using the Kaplan-Meier method and analyzed by the log rank test. The tumor-free survival rates were significantly different between the control and *Dct*-Cre *Nras*$^{Q61R/Q61R}$ groups ($p < 0.0001$) and between the control and *Dct*-Cre *Nras*$^{Q61R/+}$ groups ($p < 0.0001$).

(B) The incidence of *Nras*^{Q61R} mutation-driven melanomas was measured in tamoxifen-induced *Tyr*-CreER^{T2} *Nras*$^{Q61R/Q61R}$ mutant (green, n = 22), *Tyr*-CreER^{T2} *Nras*$^{Q61R/+}$ mutant (red, n = 23), and *Tyr*-CreER^{T2} control (blue, n = 20) mice. Statistical significance was defined as $p < 0.05$.

(C–G) *Dct*-Cre *Nras*^{Q61R} tumor sections were immunostained for S100 (C, green), SOX10 (C, red), PCNA (D, green), Ki67 (D, red), *Nras*^{Q61R} (E, brown), p-MEK (F, brown), or p-ERK (G, brown).

(H) Melanocytic markers, including S100, SOX10, MITF, MelanA/MART-1, and HMB45, were assessed by immunostaining in *Dct*-Cre *Nras*^{Q61R} tumor samples, and the percentage of positive samples for each marker was calculated.

(I) *Tyr*-CreER^{T2} *Nras*^{Q61R} tumor samples were examined using an antibody against *Nras*^{Q61R}, and the percentage of *Nras*^{Q61R}-positive samples was calculated.

(J–N) (J and K) H&E stained histological images of human melanomas. (L–N) H&E stained histological images of *Nras*^{Q61R} mutation-driven murine melanomas. Histologic images at low and high magnifications are shown (J and L, 20×) (K and M, 400×; N, 100×). The infiltrate of human primary malignant melanomas replaces the entire dermis as a sheet, punctuated by nidi of inflammation (J, yellow arrows). The nuclear-to-cytoplasmic ratios, hyperchromatic nuclei, and sometimes multiple nucleoli are shown (K, yellow arrow). The atypical mitotic figure is visible (K, green arrow). The infiltration of murine melanoma can be observed in the ear as a sheet of tumor cells, encircling the cartilage (L, yellow arrow). Severe pleomorphism of the murine melanoma cells, with large nuclear-to-cytoplasmic ratios, hyperchromatic nuclei, and intranuclear vacuoles (M, yellow arrow), and mitotic activity, (M, green arrows) is observed. The murine melanoma abuts the epidermis, with no grenz zone (N, yellow arrow), and invades the hair follicle adventitia (N, orange arrow). The extravasation of red blood cells (N, red arrow), a common finding in human melanoma, is also detected.

See also Figures S3 and S4.

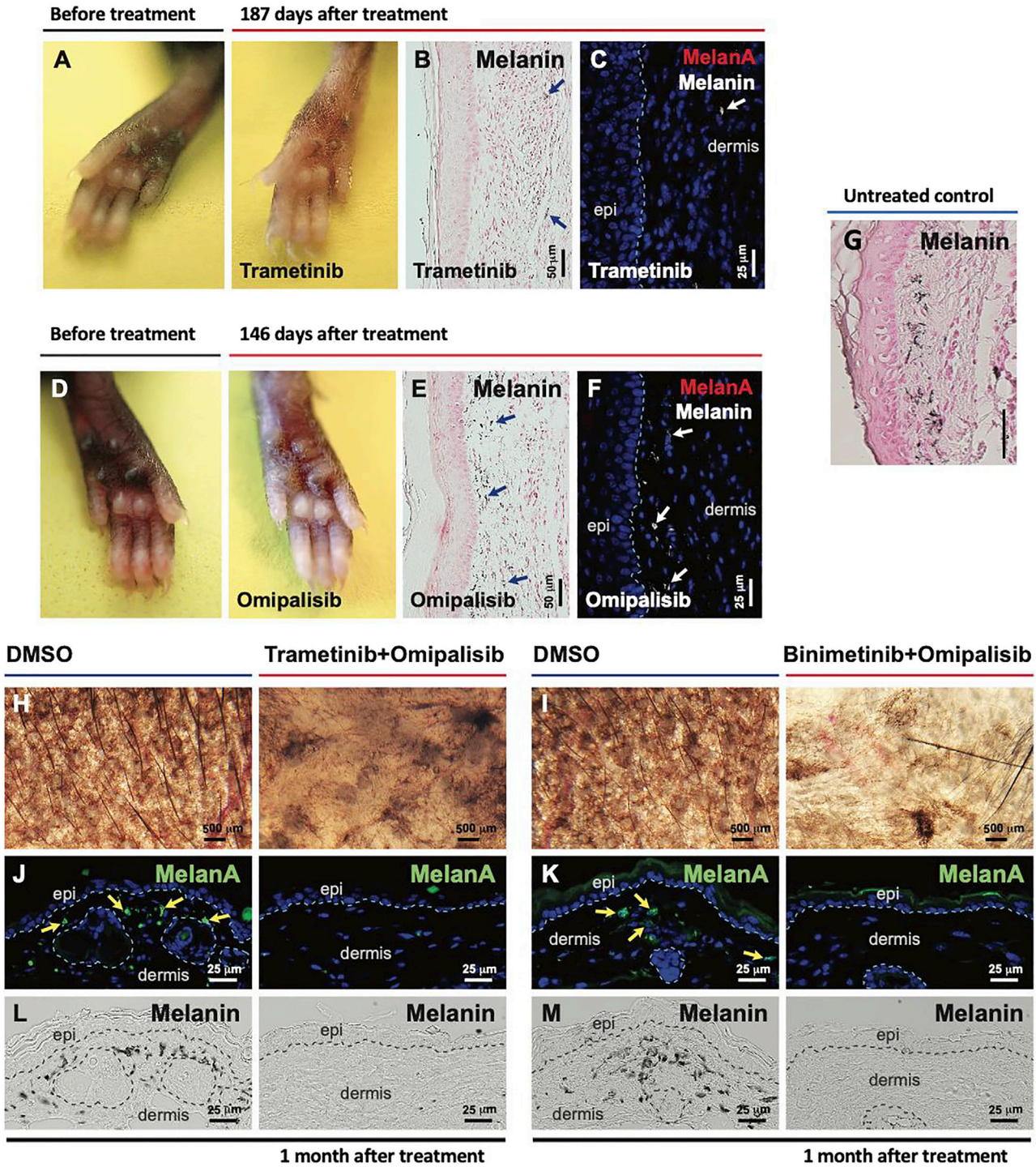

Figure 4. Local therapy with small molecule inhibitors of the NRAS signaling pathway regress *Nras*^{Q61R}-driven melanocytic nevi

(A–F) *Nras*^{Q61R} mutation-driven nevi were induced in *Tyr*-CreER^{T2} LSL-*Nras*^{Q61R} newborn mice with tamoxifen over the first postnatal week, and 2 months later, local treatments of senescent nevi were initiated with MEK and/or PI3K inhibitors or DMSO vehicle control. Trametinib (A–C, 0.1 μg/μL) or omipalisib (D–F, 0.03 μg/μL) was subcutaneously injected into the pigmented paws of tamoxifen-induced *Tyr*-CreER^{T2} *Nras*$^{Q61R/+}$ heterozygous mutants in 10 μL of 10% DMSO, three times per week for 2 weeks. Paws were visualized 187 days after treatment with trametinib (A) or 146 days after treatment with omipalisib (D). Melanin (B and E, blue arrows) was detected by Fontana-Masson staining. Tissue sections were stained for MelanA/MART1 (C and F). White arrows (in C and F) indicate dermal melanin detected by bright-field microscopy.

(legend continued on next page)

mutation-driven giant congenital nevi, as evidence supporting this for MEK inhibitors has been previously reported (Kinsler et al., 2017; Mir et al., 2019; Pawlikowski et al., 2015; Rouillé et al., 2019). We tested MEK and/or PI3K inhibitors applied as direct intralesional injection into paws (skin is thicker) or topical application to ears (Table S1). Local administration of these agents to 2-month-old tamoxifen-induced *Tyr*-CreER^{T2} *Nras*^{Q61R} mice led to a significant loss of nevus cells and hypopigmentation (Figures 4 and S5). In topical single-drug therapies, the MEK inhibitor, binimetinib, induced clear hypopigmentation (Figure S5B), and the PI3K inhibitor, omipalisib, caused moderate hypopigmentation in the dermis (Figure S5C). Subcutaneous injection of the MEK inhibitors, such as trametinib (Figures 4A and 4B) and binimetinib (Figures S5A and S5B), or of the PI3K inhibitor, omipalisib (Figures 4D, 4E, and S5C), resulted in hypopigmentation and almost complete loss of melanocytes (Figures 4C and 4F), compared with untreated control (Figure 4G). These data suggest that localized treatment of postsenescent nevi with inhibitors targeting kinases downstream of RAS may cause the selective loss of nevus cells, albeit not necessarily complete ablation. Drukker et al. showed activated AKT pathway activity in giant nevi (Drukker et al., 2013). We therefore tested various kinase-targeting combinations. When applied to right ear skin and compared with contralateral ears treated with vehicle control, we observed that topical combinations of trametinib and omipalisib (Figures 4G, 4I, and 4K) or binimetinib and omipalisib (Figures 4H, 4J, and 4L) led to strong melanocyte regression and dramatic depigmentation, demonstrating that the effects were localized and not systemic. MEK- or PI3K-targeted local therapies alone or in combination may thus regress *Nras*^{Q61R}-driven nevi. The c-KIT inhibitor, imatinib, has inhibitory effects on human melanocytes and infrequently causes skin hypopigmentation (Cerchione et al., 2009; Hemesath et al., 1998; Nishimura et al., 2002; Tsao et al., 2003; Wehrle-Haller, 2003; Wu et al., 2000; Yoshida et al., 2001). We found that single-drug treatment with imatinib resulted in measurable depigmentation (Figure S5K). Moreover, a topical combination of binimetinib with imatinib led to more profound melanocyte regressions (Figures S5F and S5G) and depigmentation (Figures S5D and S5E). This combination induced immune responses (Figures S5H–S5J), as evident by the increased inflammatory cell recruitment (CD11c+, CD163+, and CD16+) to treated lesions.

Topical squaric acid dibutylester induces local inflammation and nevus cell destruction

We chose to test the efficacy of haptens, as these are low molecular weight chemicals that become antigenic when bound to a carrier molecule and consequently elicit a well-known "contact hypersensitivity"-like response (Chipinda et al., 2011; Vocanson et al., 2009). To determine whether topical hapten-based immunotherapy is capable of regressing congenital nevi, we tested SADBE, as a single-agent topical immunotherapy. SADBE was chosen for this study because it is already clinically used by dermatologists as a topical agent for alopecia areata and warts and because it has been described to induce hypopigmentation or vitiligo (Sakai et al., 2020; Silverberg et al., 2000; Valsecchi et al., 1989). 2 months after tamoxifen induction of nevi in ear skin of *Tyr*-CreER^{T2} *Nras*^{Q61R} neonatal mice, the *Nras*^{Q61R} mutation-driven nevus mice were sensitized by applying 2% SADBE to the right side of the shaved abdomen. Subsequent treatment of the right ear with topical 1.5% SADBE occurred three times over the following week. This short-term single-agent therapy resulted in major regression of congenital nevi (Figure 5A). We next tested the efficacy of SADBE single agent on both senescent and proliferative giant congenital nevi in dorsal skin of *Dct*-Cre *Nras*^{Q61R}-mutant mice as depicted in Figures 5B and 5G, respectively. When senescent nevus lesions were treated with SADBE beginning at 2 months of age, we observed skin depigmentation in areas treated with SADBE (Figures 5C and 5F). This regression was confirmed by the disappearance of both melanocytes and melanin (Figures 5D and 5E). To study susceptibility of proliferative nevi, SADBE treatments were initiated within a week of birth as depicted in Figure 5G, prior to the loss of proliferative nevus features (Figure 2E). Nevus regression was again noted (Figure 5H, lower panel red arrow) as well as subsequent leukotrichia (white hair) in SADBE-treated areas (Figure 5H, upper panel red arrow). In contrast, melanocytic nevi remained in areas treated with vehicle control (Figure 5H, purple arrows). Disappearance of both melanocytes and melanin was verified in treated lesions (Figures 5I and 5J).

Topical squaric acid dibutylester regression of nevi involves recruitment and M1-like polarization of macrophages

In order to assess immune cell requirements for the SADBE-dependent regression of nevi, depletion of specific immune populations was performed on 2-month-old *Dct*-Cre *Nras*^{Q61R} mice through IP injection of monoclonal antibodies directed at distinct immune lineages. Skin Melan-A-positive nevus cells were quantified after SADBE treatment and compared with vehicle control (Figure 6A). Depletion of macrophages via anti-F4/80 significantly inhibited the ability of SADBE to clear melan-A-positive cells; however, depletion of CD4+ T cells, NK1.1+ NK cells CD8+ T cells, and CD19+ B cells did not

(G) Representative image of melanin detected by Fontana-Masson staining of nontreated tamoxifen-induced *Tyr*-CreER^{T2} *Nras*$^{Q61R/+}$ mice from postnatal day 16, 2 weeks after tamoxifen induction.

(H–M) Topical combinatorial therapies. Topical combinatorial therapies with the PI3K inhibitor, omipalisib (10 μg/μL), plus the MEK inhibitor, trametinib (H, J, and L, 2 μg/μL) or binimetinib (I, K, and M, 10 μg/μL), were applied to the pigmented ears of tamoxifen-induced *Tyr*-CreER^{T2} *Nras*$^{Q61R/Q61R}$-mutant mice. All topical agents were administered in 5 μL DMSO, five times per week for 3 weeks ("Trametinib+Omipalisib" and their vehicle control treatments) or for 6 weeks ("Binimetinib+Omipalisib" and their vehicle control treatments). Ear skin tissues were harvested 1 month after the final drug treatment, and nevus regression was examined. Images were obtained with a stereomicroscope, and the dark brown particles indicate melanin (H and I). Tissue sections were stained for MelanA/MART1 (J and K, green). Yellow arrows indicate positive signals. Dermal melanin detected by bright-field microscopy is shown (L and M, black). We used five mice per treatment group, and representative images are shown.

See also Figure S5.

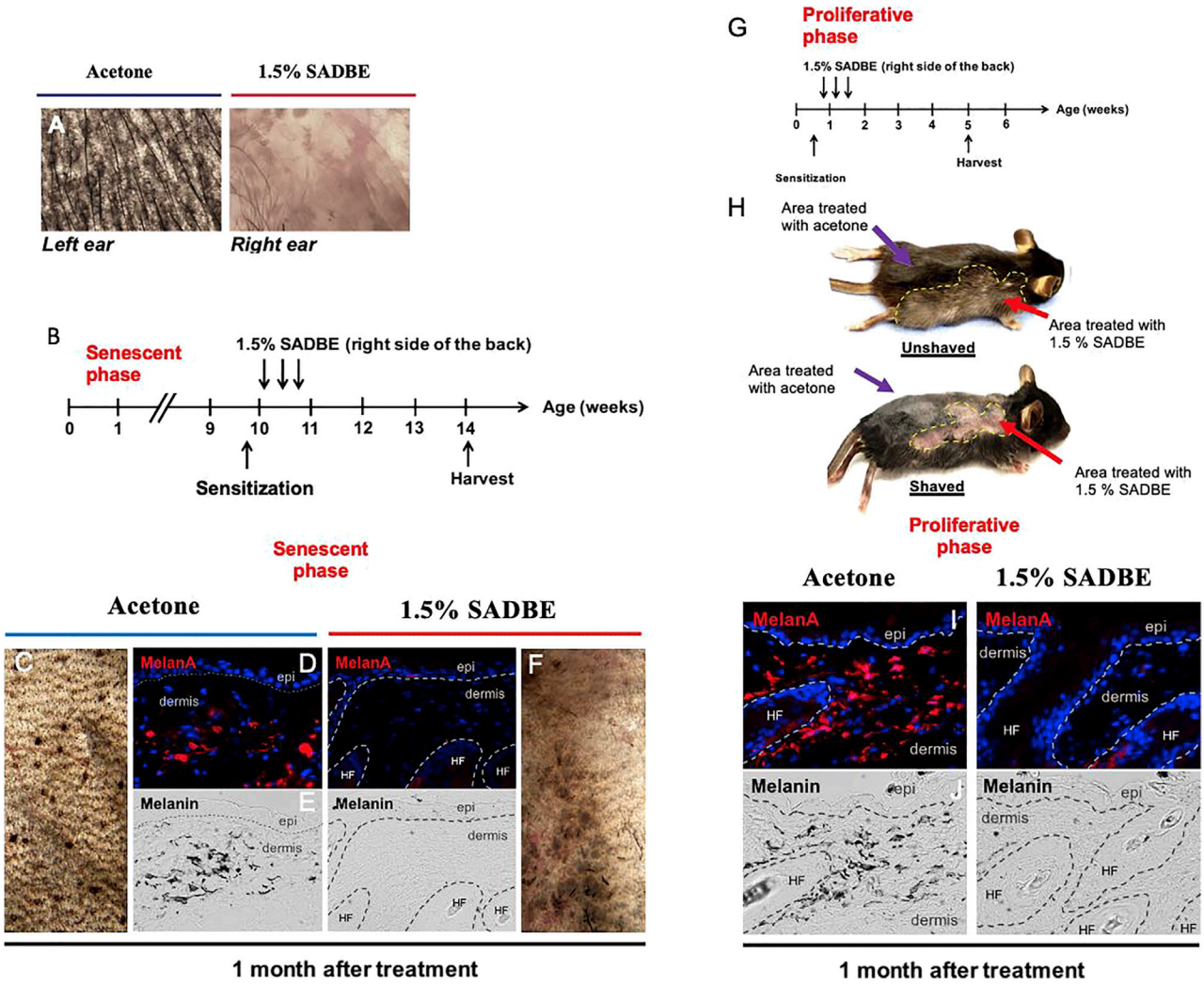

Figure 5. Single-agent local immunotherapy with topical SADBE results in significant regression of both neonatal proliferative and postnatal senescent congenital nevi

(A) SADBE (1.5%, topical) was applied to the pigmented right ears of tamoxifen-induced *Tyr*-CreER^{T2} *Nras*$^{Q61R/Q61R}$ mutant mice 2 months after tamoxifen induction, whereas the pigmented left ears of the same animals were treated with acetone vehicle. Ear tissue images were obtained with a stereomicroscope, and dark brown particles indicate melanin.

(B–J) (B) Treatment scheme of adult *Dct*-Cre *Nras*$^{Q61R/Q61R}$. Single-drug local therapy with 1.5% SADBE was administered topically to the right back. Acetone was applied topically to the left back of each SADBE-treated mouse as a vehicle control. All treatments were carried out three times per week (every other day), and the treated skin tissues were harvested 1 month after the first treatment to assess regression of melanocytic nevi (C and F). Tissue sections were immunostained for MelanA/MART1 (D and I). Melanin (black) detected by bright-field microscopy is shown in (E) and (J). (G) Treatment scheme of neonatal *Dct*-Cre *Nras*$^{Q61R/Q61R}$ mice. (H) Representative images of treated *Dct*-Cre *Nras*$^{Q61R/Q61R}$ mice unshaved (upper panel) and shaved (lower panel) are shown. White hairs were detectable in treated areas (H, upper panel red arrow). Regression of melanocytic nevi was detectable in treated areas (H, lower panel red arrow). The purple arrows in (H) indicate unchanged nevi in the nevus lesion treated with acetone vehicle. Yellow-dashed lines in (H) demarcate the region treated with 1.5% SADBE. Stippled white lines in (D), (E), (I), and (J) separate the epidermis (epi) and hair follicles (HF) from the dermis.

diminish the regression efficacy of SADBE. Depletion of tissue-resident cells (such as macrophages) is typically incomplete compared with other hematopoietic lineages, but the diminished efficacy of SADBE despite incomplete depletion (Figure 6B) strongly suggests that these cells play a key functional role in nevus clearance. Cells expressing the proinflammatory macrophage (M1) marker iNOS (inducible nitric oxide synthase) were also strongly recruited by SADBE (Figure 6B), as were anti-inflammatory Arg1+ cells (Figure 6C). Furthermore, CD4+ T cell depletion enhanced macrophage recruitment, with modestly larger increases in proinflammatory (and decreased anti-inflammatory Arg1+) populations and slightly higher melanin clearance (Figure 6C). Thus, SADBE appears to attract both inflammatory and anti-inflammatory macrophages. To independently assess the effect of SADBE on the presence of markers for these cell populations, *Dct*-Cre *Nras*^{Q61R} mice were treated with either SADBE or vehicle control (3 per treatment or control groups) for 72 h, and

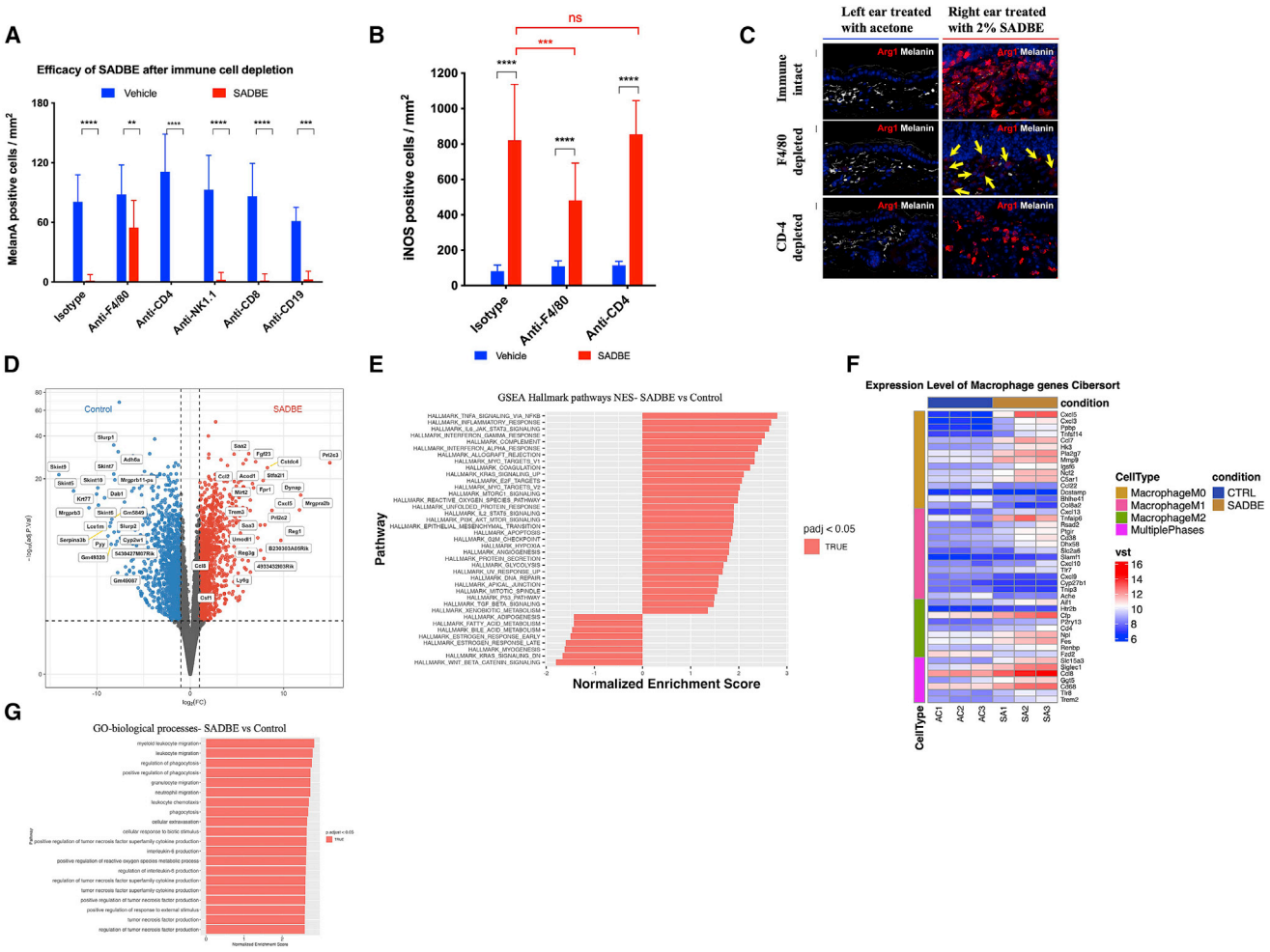

Figure 6. Antibody-mediated depletion of inflammatory cell lineages in mice and RNA-seq reveal macrophage recruitment by SADBE

(A) Quantification of Melan-A-positive cells per mm^2 in *Dct*-Cre *Nras*^{Q61R} mice after immunodepletion by IP injection with 750 μg of anti-F4/80, anti-CD-4, anti-NK1.1, anti-CD-8, and anti-CD-19.

(B) Quantification of iNOS positive cells per mm^2 in *Dct*-Cre *Nras*^{Q61R} mice after immunodepletion by IP injection with 750 μg of anti-F4/80 and anti-CD-4.

(C) Arg1 staining (red) of ear skin sections following depletion with anti-CD-4, anti-F4/80, isotype control, and 2% SADBE treatment for 1 week. Yellow arrows indicate negative signals. Melanin detected by bright-field microscopy is shown in white.

(D) Differential gene expression analysis.

(E) GSEA hallmark pathways analysis.

(F) Heatmap of macrophage marker groups according to macrophage phase.

(G) GO biological processes analysis. *Dct*-Cre *Nras*^{Q61R} mice were treated with SADBE (2%) or vehicle control (acetone) on dorsal skin (3 mice per treatment or control group). Whole-skin RNA-seq was performed 72 h after treatment. Macrophage-associated genes for M0, M1, and M2 phases were collected from the hematopoietic gene signature set LM22.

RNA-seq was carried out. Differential gene expression analysis revealed macrophage-related cytokines among top upregulated genes (Figure 6D). GSEA analysis showed TNFα (tumor necrosis factor α) signaling via NF-κB (nuclear factor kappa-light-chain-enhancer of activated B cells) as the top upregulated pathway (Figure 6E). SADBE was shown to highly induce genes of multiple macrophage subtypes, which included proinflammatory M1-like polarization genes (Figure 6F) and GO (gene ontology) biological processes analysis showed migration and regulation of phagocytosis as enriched pathways (Figure 6G).

Topical squaric acid dibutylester decreases nevus cell numbers in human CMN xenografts

These lineage-ablation and expression studies suggested that SADBE's clearance of nevus cells was not dependent upon adaptive immune cell types but rather required macrophage function. We therefore engrafted human discarded resected CMN tissue onto immunodeficient SHO mice (which lack adaptive immunity but retain at least partial macrophage function) (Bancroft and Kelly, 1994; Charles River) in order to test responses to SADBE. Eight human CMN xenografts were thus generated from a single giant nevus specimen. We utilized the

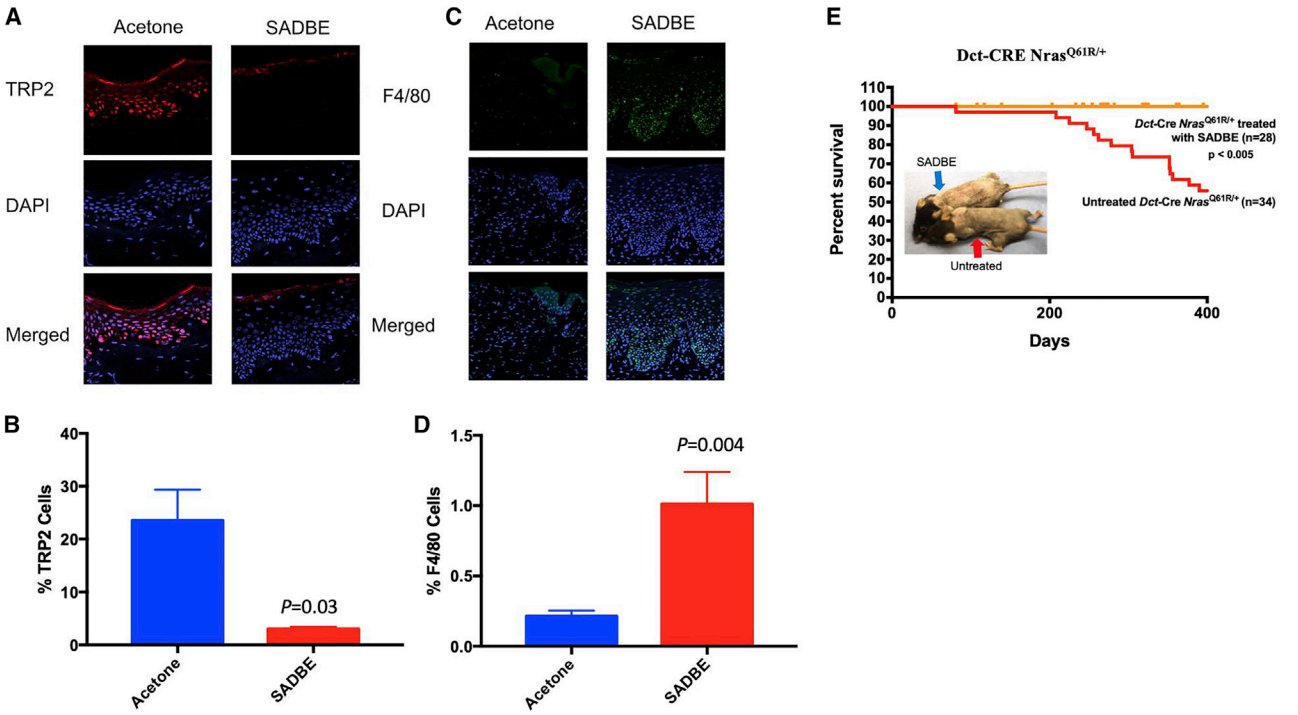

Figure 7. SADBE decreases melanocyte numbers in CMN xenografts and prevents melanoma formation in mice

(A) Immunofluorescent staining of CMN tissue xenografts treated with topical application of 1% SADBE or acetone control for 8 months: DAPI (blue) TRP2 (red) Merged (purple).

(B) Quantification of the percentage of TRP2 positive cells of the total cells in the epidermis.

(C) Immunofluorescent staining of CMN tissue xenografts treated with topical application of 1% SADBE or acetone control for 2 weeks: DAPI (blue) F4/80 (green) Merged (cyan).

(D) Quantification of F4/80 positive cells as percent of total cells.

(E) Effect of SADBE on melanoma genesis and mouse survival in Dct-Cre *Nras*$^{Q61R/+}$ mice. Mice were sensitized with a 2% SADBE in acetone treatment of the right side of the shaved abdomen. 3 days later, sensitized mice were treated with 1.5% SADBE over the shaved dorsal (back) skin (treated and untreated controls indicated by arrows). Treatments with SADBE were carried out every other day (total of three treatments), and tumor formation was monitored. Untreated control tumor incidences are the same (historical) control *Dct*-CRE *Nras*$^{Q61R/+}$ mice in Figure 3A. In a population where anatomic location was tracked, dorsal back specific melanomas occurred in 13 of 21 (61.9%) control mice. See also Figure S6.

epidermal region of the lesion that contained a significant epidermal nevus component for engraftment, thereby enhancing vascular supply and immune access. Following a 4-month recovery period, the grafts were subjected to biweekly topical treatment with 1% SADBE (or vehicle control) with dosing guided by potential sensitivity of the graft, followed by harvesting and staining for nevus cells using the melanocytic antibody anti-TRP2 (TRP, transient receptor potential). SADBE treatments in these xenografted mice led to thickening of the stratum corneum (superficial dead cell layer of xenografts, Figure S6A), which contained significantly accumulated pigment, thus obscuring underlying cellular pigmentation changes. Stratum corneum thickening was not observed in mouse models (above) or in humans who were treated with SADBE for warts or alopecia areata. Immunofluorescence staining and automated quantification of underlying nevus cells (TRP2+) revealed a striking melanocyte decrease of ~90% ($p = 0.03$) in human giant nevus xenografts following SADBE treatment as compared with vehicle controls (Figures 7A and 7B). To further examine whether SADBE treatments of human-to-mouse xenografts were inducing macrophage recruitment (as in the murine model), specimens from 2 weeks following initiation of topical SADBE treatment were stained with the macrophage marker F4/80. Figures 7C and 7D depict the results of F4/80+ immunostaining and its quantification and reveal significant recruitment of mouse macrophages (F4/80+) into the CMN tissue (vehicle 0.21 ± 0.03, SADBE 1.01 ± 0.22, $p = 0.004$). These results corroborate nevus cell regressions within human tissue, showing that SADBE exhibits the ability to induce macrophage recruitment together with the significant clearance of human CMN cells within the murine SHO model.

SADBE prevents melanoma formation in *Nras*^{Q61R} mice

To more stringently test whether SADBE could visually regress melanocytic nevus cells, regress pigmentation, and also prevent melanoma formation, we treated a cohort of 29 *Dct*-Cre *Nras*$^{Q61R/+}$ mice with SADBE over dorsal trunk skin and observed their long-term melanoma incidence for up to 400 days. As shown in Figure 7E, pretreatment with SADBE fully protected against melanoma formation within the treated skin (dorsal half

of the trunk) during the observation period. Importantly, six melanomas did form in the SADBE-treated mice; however, all of these tumors were in untreated areas of the skin, where depigmentation was also not observed (Figure 7E, blue arrow), further confirming the localized activity of the regressive treatment. Finally, to determine whether lower doses of SADBE may be capable of minimizing toxicity while maintaining efficacy at regressing CMN cells in the *Dct-Nras*^{Q61R} model, we tested the lower dose 0.5% SADBE 3 times per week for 6 total doses (2 weeks) rather than 1.5% for 3 doses. We observed similar depigmentation with the lower dose of SADBE (Figure S6B), suggesting that additional dose/schedule options should be pursued before future application of this strategy.

DISCUSSION

We report the development of a collection of engineered murine models for giant congenital nevi, which permit us to distinguish proliferative from senescent phases of these lesions. These preclinical models complement previously reported *Nras*-transgenic models (Ackermann et al., 2005; Shakhova et al., 2012) and permitted the identification of multipronged therapeutic approaches for nonsurgical regression of the lesions and prevention of melanoma formation. These data suggest potentially valuable treatment strategies for children with giant congenital nevi morbidity, which otherwise lack effective nonsurgical therapies. Along with alleviating the cosmetic and psychosocial effects of giant congenital melanocytic nevi (Koot et al., 2000; Price and Schaffer, 2010; Tromberg et al., 2005), a driving purpose of this study is to diminish the increased melanoma risk arising from these lesions, as was strongly observed following 1 week (3 treatments) of topical SADBE in our mouse models. It is important to note that the melanoma risk in patients with CMN is not fully confined to cutaneous locations, as deeper melanocytic populations may exist, due to differences in the developmental states in which the nevus formed (oncogenic mutation). Nonetheless, cutaneous melanomagenesis is a significant challenge in these patients and likely contributes importantly to current parental decisions to seek debilitating surgical resections. The plausibility of exploiting the proinflammatory hapten SADBE is supported by its active use in several unrelated clinical contexts (Happle et al., 1980; Micali et al., 2000) as well as anecdotal reports of vitiligo-like depigmentation in humans, where the agent was used topically for other indications such as alopecia areata (Sakai et al., 2020; Valsecchi et al., 1989). Although SADBE achieved melanocyte clearance, we emphasize the value in further interrogating kinase-targeting agents that, despite requiring further development as local-cutaneous drugs, offer potential advantages of specific molecular targeting. Mechanistically, melanocyte clearance utilizes recruitment of macrophages into the skin. Other studies in mice (Feng et al., 2017; Gupta et al., 2006; Zöller et al., 2004) and a human case report (Herrmann et al., 2004) have demonstrated macrophage recruitment by haptens suggesting that the macrophage recruitment observed here is unlikely to be particular to nevi or SADBE. Our RNA-seq data of SADBE-treated mice revealed multiple macrophage cytokines, such as CCL2 (Fuentes et al., 1995; Rollins, 1991) and CCL7 (Xuan et al., 2015) as well as the monocyte recruiting chemokine CCL8 (Ji et al., 2019) and macrophage differentiating cytokine CSF (colony stimulating factor)-1 (Jones and Ricardo, 2013), which may contribute to macrophage recruitment to the treated area. Furthermore, the TNFα signaling pathway was found to be highly upregulated after SADBE treatment. TNFα can elevate cytotoxic activity of macrophages (Salim et al., 2016). Interestingly, TNFα is also able to affect both the growth and melanogenesis of melanocytes (Englaro et al., 1999; Hu et al., 2002). In addition, increased levels of TNFα were found in vitiligo lesions, and exposure of melanocytes to TNFα was reported to downregulate MITF-M and induces apoptosis (Singh et al., 2021). TNFα is produced predominantly by macrophages (Riches et al., 1996). Therefore, TNFα induction represents a candidate mechanism of melanocyte/nevocyte reduction either by elevating cytotoxic activity of macrophages or by inducing melanocyte apoptosis. Since our GO analysis revealed phagocytosis as an enriched pathway, this process may participate in nevus clearance. Our functional data demonstrated that macrophage depletion impeded SADBE's efficacy at nevus regression, and we believe future studies could further clarify exactly which macrophage functions contribute to this activity. In our studies, manipulations favoring proinflammatory macrophages enhanced melanocyte clearance, suggesting that future strategies to modulate this macrophage population might further refine the selectivity of the treatment. Interestingly, our LISA analysis and GSEA pathway analysis revealed many transcription factors involved in immune system and interferon-α pathway activity to be highly regulated in both mouse and human CMN. This could be as a result of the senescent characteristics of the nevi that can induce the senescence-associated secretory phenotype (Coppé et al., 2010). Given clinical anecdotes of melanocyte loss after SADBE in settings independent of CMN, these findings suggest potential applications for other conditions where melanocyte clearance may be beneficial, such as cases where distinct driver oncogenes drive melanocytic neoplasia. Collectively, this study provides preclinical genetically driven and human-engrafted congenital nevus models that show translational potential for future human clinical testing.

Limitations of the study

In this proof-of-principle study, several murine models of congenital giant nevi are developed, and various treatments are tested to regress the lesions. However, there are several limitations. They are as follows:

(1) Although genetically matching the *NRAS*^{Q61R} gene driving many human CMNs, the nevi are present within mouse skin that differs structurally from human skin. For example, interfollicular dorsal skin in mice does not normally contain melanocytes, and ear skin, which does contain epidermal melanocytes in mouse, is particularly thin, lacking barrier features of human skin.
(2) A variety of kinase-targeting agents demonstrated significant regressions of the CMN cells in the mouse CMN lesions. However, these agents have not been developed for either topical or injected cutaneous delivery. Therefore, the feasibility of delivering these agents into human skin awaits further study.

(3) SADBE efficiently regresses CMN cells in several of the genetically engineered mouse CMN models. However, it is unknown how the relative dosing of SADBE in mouse will apply to humans, a question which requires additional evaluation.
(4) SADBE also regressed ~90% of human CMNs within resected human CMN specimens, xenografted onto immunodeficient mice, and recruited macrophages into the CMN xenografts. However, the immunodeficient background of the xenograft recipients remains an imperfect predictor of *in vivo* responses in immune-intact human skin.

STAR★METHODS

Detailed methods are provided in the online version of this paper and include the following:

- KEY RESOURCES TABLE
- RESOURCE AVAILABILITY
  - Lead contact
  - Materials availability
  - Data and code availability
- EXPERIMENTAL MODEL AND SUBJECT DETAILS
  - Ethics Statement
  - Mice
- METHOD DETAILS
  - Animal studies and analysis of melanoma incidence
  - Quantification of proliferative and senescent phases
  - Quantification of Melan A or iNOS positive cells
  - Treatment procedures for therapeutic agents
  - Histology, staining, and imaging
  - *Nras* loss of heterozygosity
  - *In vivo* depletion of immune cells
  - RNA-Sequencing of SADBE treated samples
  - RNA-Sequencing mouse model comparison
  - RNA-Sequencing Analysis
  - Transplantation of CMN xenografts
  - SADBE treatment of xenografts
  - Imaging of CMN xenografts
- QUANTIFICATION AND STATISTICAL ANALYSIS

SUPPLEMENTAL INFORMATION

Supplemental information can be found online at https://doi.org/10.1016/j.cell.2022.04.025.

ACKNOWLEDGMENTS

The authors gratefully acknowledge the original sources of key mouse strains by Dr. Lionel Larue, Institut Curie, Paris, France (*Tyr* promoter-driven Cre), Dr. Friedrich Beermann, Swiss Institute for Experimental Cancer Research, Epalinges, Switzerland (*Dct*-CRE), and Dr. Marcus Bosenberg, Yale University (*Tyr*-CreERT2, tamoxifen inducible). The authors gratefully acknowledge support from NIH: (D.E.F.) R01AR072304, (D.E.F.) R01AR043369, (D.E.F. and X.S.L.) P01CA163222, and (D.E.F.) R01CA222871; (D.E.F.) the Dr. Miriam and Sheldon G. Adelson Medical Research Foundation; and (J.L.C.) the MGH Summer Research Trainee Program. The graphical abstract was created with biorender.com.

AUTHOR CONTRIBUTIONS

D.E.F. conceived and directed the study. Y.S.C., T.H.E., and D.E.F. designed the experiments and analyzed and interpreted the data. Y.S.C., T.H.E., M.v.F., I.R., J.L.F., M.P.d.S., A.S.D., S.L., O.F., J.L.C., Y.L.S., and E.F. performed the animal experiments, including tumor studies, molecular analyses, and histological analyses. Y.Z., A.J., T.H.E., M.S., S.R., D.S.H., and X.S.L. performed and analyzed the RNA-seq data. E.B.S., I.R., and S.D. designed and transplanted the xenografts experiments. C.E.B. and N.E.S. contributed precious unpublished reagents. W.G.A., B.B., C.L.C., L.R.Z., and M.C.M. contributed clinical samples and interpreted histologic diagnoses. S.G. generated reagents and provided intellectual input. Y.S.C., T.H.E., and D.E.F. wrote the manuscript with input and edits from all co-authors.

DECLARATION OF INTERESTS

D.E.F. has a financial interest in Soltego, a company developing salt inducible kinase inhibitors for topical skin-darkening treatments that might be used for a broad set of human applications. The interests of D.E.F. were reviewed and are managed by Massachusetts General Hospital and Partners HealthCare in accordance with their conflict-of-interest policies.

C.L.C. has a financial interest in 4Immune, a company developing cell therapy treatments that can be used for a broad set of human applications. The interests of C.L.C were reviewed and are managed by Mass General Brigham in accordance with their conflict-of-interest policies.

X.S.L. is a cofounder, board member, SAB member, and consultant of GV20 Oncotherapy and its subsidiaries; stockholder of BMY, TMO, WBA, ABT, ABBV, and JNJ; and received research funding from Takeda, Sanofi, Bristol Myers Squibb, and Novartis. M.C.M. discloses consulting relationship with Novartis, Advisory Board with BioCoz and Caliber ID, and author royalties with Wiley & Sons.

Received: January 5, 2022
Revised: March 28, 2022
Accepted: April 15, 2022
Published: May 12, 2022

REFERENCES

Ackermann, J., Frutschi, M., Kaloulis, K., McKee, T., Trumpp, A., and Beermann, F. (2005). Metastasizing melanoma formation caused by expression of activated N-RasQ61K on an INK4a-deficient background. Cancer Res *65*, 4005–4011. https://doi.org/10.1158/0008-5472.CAN-04-2970.

Bajaj, M.S., Khuraijam, N., Sen, S., and Pushker, N. (2009). Congenital melanocytoma manifesting as proptosis with multiple cutaneous melanocytic nevi and oculodermal melanosis. Arch. Ophthalmol. *127*, 937–939. https://doi.org/10.1001/archophthalmol.2009.146.

Bancroft, G.J., and Kelly, J.P. (1994). Macrophage activation and innate resistance to infection in SCID mice. Immunobiology *191*, 424–431. https://doi.org/10.1016/S0171-2985(11)80448-1.

Bauer, J., Curtin, J.A., Pinkel, D., and Bastian, B.C. (2007). Congenital melanocytic nevi frequently harbor NRAS mutations but no BRAF mutations. J. Invest. Dermatol. *127*, 179–182. https://doi.org/10.1038/sj.jid.5700490.

Bett, B.J. (2005). Large or multiple congenital melanocytic nevi: occurrence of cutaneous melanoma in 1008 persons. J. Am. Acad. Dermatol. *52*, 793–797. https://doi.org/10.1016/j.jaad.2005.02.024.

Bosenberg, M., Muthusamy, V., Curley, D.P., Wang, Z., Hobbs, C., Nelson, B., Nogueira, C., Horner, J.W., 2nd, Depinho, R., and Chin, L. (2006). Characterization of melanocyte-specific inducible Cre recombinase transgenic mice. Genesis *44*, 262–267. https://doi.org/10.1002/dvg.20205.

Burd, C.E., Liu, W., Huynh, M.V., Waqas, M.A., Gillahan, J.E., Clark, K.S., Fu, K., Martin, B.L., Jeck, W.R., Souroullas, G.P., et al. (2014). Mutation-specific RAS oncogenicity explains NRAS codon 61 selection in melanoma. Cancer Discov *4*, 1418–1429. https://doi.org/10.1158/2159-8290.CD-14-0729.

Cerchione, C., Fabbricini, R., Pane, F., and Luciano, L. (2009). Vitiligo-like lesions in an adult patient treated with imatinib mesylate. Leuk. Res. *33*, e104–e105. https://doi.org/10.1016/j.leukres.2008.12.023.

Charbel, C., Fontaine, R.H., Malouf, G.G., Picard, A., Kadlub, N., El-Murr, N., How-Kit, A., Su, X., Coulomb-L'Hermine, A., Tost, J., et al. (2014). NRAS mutation is the sole recurrent somatic mutation in large congenital melanocytic nevi. J. Invest. Dermatol. *134*, 1067–1074. https://doi.org/10.1038/jid.2013.429.

Chien, J.C., Niu, D.M., Wang, M.S., Liu, M.T., Lirng, J.F., Chen, S.J., and Hwang, B. (2010). Giant congenital melanocytic nevi in neonates: report of two cases. Pediatr. Neonatol. *51*, 61–64. https://doi.org/10.1016/S1875-9572(10)60012-5.

Chipinda, I., Hettick, J.M., and Siegel, P.D. (2011). Haptenation: chemical reactivity and protein binding. J. Allergy (Cairo) *2011*, 839682. https://doi.org/10.1155/2011/839682.

Coppé, J.P., Desprez, P.Y., Krtolica, A., and Campisi, J. (2010). The senescence-associated secretory phenotype: the dark side of tumor suppression. Annu. Rev. Pathol. *5*, 99–118. https://doi.org/10.1146/annurev-pathol-121808-102144.

Delmas, V., Martinozzi, S., Bourgeois, Y., Holzenberger, M., and Larue, L. (2003). Cre-mediated recombination in the skin melanocyte lineage. Genesis *36*, 73–80. https://doi.org/10.1002/gene.10197.

Dobin, A., Davis, C.A., Schlesinger, F., Drenkow, J., Zaleski, C., Jha, S., Batut, P., Chaisson, M., and Gingeras, T.R. (2013). STAR: ultrafast universal RNA-seq aligner. Bioinformatics *29*, 15–21. https://doi.org/10.1093/bioinformatics/bts635.

Drukker, L., Margulis, A., Chaouat, M., Levitzki, R., Maiorenko, E., and Ben Bassat, H. (2013). Changes of PI3K/AKT/BCL2 signaling proteins in congenital Giant Nevi: melanocytes contribute to their increased survival and integrity. J. Recept. Signal Transduct. Res. *33*, 359–366. https://doi.org/10.3109/10799893.2013.838785.

Englaro, W., Bahadoran, P., Bertolotto, C., Buscà, R., Dérijard, B., Livolsi, A., Peyron, J.F., Ortonne, J.P., and Ballotti, R. (1999). Tumor necrosis factor alpha-mediated inhibition of melanogenesis is dependent on nuclear factor kappa B activation. Oncogene *18*, 1553–1559. https://doi.org/10.1038/sj.onc.1202446.

Feng, J., Yang, P., Mack, M.R., Dryn, D., Luo, J., Gong, X., Liu, S., Oetjen, L.K., Zholos, A.V., Mei, Z., et al. (2017). Sensory TRP channels contribute differentially to skin inflammation and persistent itch. Nat. Commun. *8*, 980. https://doi.org/10.1038/s41467-017-01056-8.

Fuentes, M.E., Durham, S.K., Swerdel, M.R., Lewin, A.C., Barton, D.S., Megill, J.R., Bravo, R., and Lira, S.A. (1995). Controlled recruitment of monocytes and macrophages to specific organs through transgenic expression of monocyte chemoattractant protein-1. J. Immunol. *155*, 5769–5776.

Gerami, P., and Paller, A.S. (2013). Making a mountain out of a molehill: NRAS, mosaicism, and large congenital nevi. J. Invest. Dermatol. *133*, 2127–2130. https://doi.org/10.1038/jid.2013.146.

Gray-Schopfer, V.C., Cheong, S.C., Chong, H., Chow, J., Moss, T., Abdel-Malek, Z.A., Marais, R., Wynford-Thomas, D., and Bennett, D.C. (2006). Cellular senescence in naevi and immortalisation in melanoma: a role for p16? Br. J. Cancer *95*, 496–505. https://doi.org/10.1038/sj.bjc.6603283.

Gupta, P., Freyschmidt-Paul, P., Vitacolonna, M., Kiessling, S., Hummel, S., Hildebrand, D., Marhaba, R., and Zöller, M. (2006). A chronic contact eczema impedes migration of antigen-presenting cells in alopecia areata. J. Invest. Dermatol. *126*, 1559–1573. https://doi.org/10.1038/sj.jid.5700328.

Guyonneau, L., Murisier, F., Rossier, A., Moulin, A., and Beermann, F. (2004). Melanocytes and pigmentation are affected in dopachrome tautomerase knockout mice. Mol. Cell. Biol. *24*, 3396–3403. https://doi.org/10.1128/MCB.24.8.3396-3403.2004.

Happle, R., Kalveram, K.J., Büchner, U., Echternacht-Happle, K., Göggelmann, W., and Summer, K.H. (1980). Contact allergy as a therapeutic tool for alopecia areata: application of squaric acid dibutylester. Dermatologica *161*, 289–297. https://doi.org/10.1159/000250380.

Hashmi, G.S., Ahmed, S.S., and Khan, S. (2009). Congenital giant melanocytic nevi. Rare Tumors *1*, e9. https://doi.org/10.4081/rt.2009.e9.

Hemesath, T.J., Price, E.R., Takemoto, C., Badalian, T., and Fisher, D.E. (1998). MAP kinase links the transcription factor Microphthalmia to c-Kit signalling in melanocytes. Nature *391*, 298–301. https://doi.org/10.1038/34681.

Herrmann, G., Groth, W., Krieg, T., and Mauch, C. (2004). Complete remission of Merkel cell carcinoma of the scalp with local and regional metastases after topical treatment with dinitrochlorbenzol. J Am Acad Dermatol *50*, 965–969. https://doi.org/10.1016/j.jaad.2003.11.049.

Hu, D.-N., McCormick, S., and Mehta, S. (2002). Effects of tumor necrosis factor-alpha on the growth and melanogenesis of human uveal melanocytes in vitro. Invest. Ophthalmol. Vis. Sci. *43*, 1089.

Ibrahimi, O.A., Alikhan, A., and Eisen, D.B. (2012). Congenital melanocytic nevi: where are we now? Part II. Treatment options and approach to treatment. J. Am. Acad. Dermatol. *67*, 515-.e511. 515.e513; quiz 528–530. https://doi.org/10.1016/j.jaad.2012.06.022.

Ji, J., Wang, P., Zhou, Q., Zhu, L., Zhang, H., Zhang, Y., Zheng, Z., Bhatta, A.K., Zhang, G., and Wang, X. (2019). CCL8 enhances sensitivity of cutaneous squamous cell carcinoma to photodynamic therapy by recruiting M1 macrophages. Photodiagnosis Photodyn. Ther. *26*, 235–243. https://doi.org/10.1016/j.pdpdt.2019.03.014.

Jiang, P., Gu, S., Pan, D., Fu, J., Sahu, A., Hu, X., Li, Z., Traugh, N., Bu, X., Li, B., et al. (2018). Signatures of T cell dysfunction and exclusion predict cancer immunotherapy response. Nat. Med. *24*, 1550–1558. https://doi.org/10.1038/s41591-018-0136-1.

Jones, C.V., and Ricardo, S.D. (2013). Macrophages and CSF-1: implications for development and beyond. Organogenesis *9*, 249–260. https://doi.org/10.4161/org.25676.

Kinsler, V.A., Birley, J., and Atherton, D.J. (2009). Great Ormond Street Hospital for Children Registry for congenital melanocytic naevi: prospective study 1988-2007. Part 1-epidemiology, phenotype and outcomes. Br. J. Dermatol. *160*, 143–150. https://doi.org/10.1111/j.1365-2133.2008.08849.x.

Kinsler, V.A., O'Hare, P., Jacques, T., Hargrave, D., and Slater, O. (2017). MEK inhibition appears to improve symptom control in primary NRAS-driven CNS melanoma in children. Br. J. Cancer *116*, 990–993. https://doi.org/10.1038/bjc.2017.49.

Kinsler, V.A., Thomas, A.C., Ishida, M., Bulstrode, N.W., Loughlin, S., Hing, S., Chalker, J., McKenzie, K., Abu-Amero, S., Slater, O., et al. (2013). Multiple congenital melanocytic nevi and neurocutaneous melanosis are caused by postzygotic mutations in codon 61 of NRAS. J. Invest. Dermatol. *133*, 2229–2236. https://doi.org/10.1038/jid.2013.70.

Koot, H.M., de Waard-van der Spek, F., Peer, C.D., Mulder, P.G., and Oranje, A.P. (2000). Psychosocial sequelae in 29 children with giant congenital melanocytic naevi. Clin. Exp. Dermatol. *25*, 589–593. https://doi.org/10.1046/j.1365-2230.2000.00712.x.

Korotkevich, G., Sukhov, V., Budin, N., Shpak, B., Artyomov, M., and Sergushichev, A. (2021). Fast gene set enrichment analysis. Preprint at bioRxiv, 060012.

Krengel, S., Hauschild, A., and Schäfer, T. (2006). Melanoma risk in congenital melanocytic naevi: a systematic review. Br. J. Dermatol. *155*, 1–8. https://doi.org/10.1111/j.1365-2133.2006.07218.x.

Leech, S.N., Bell, H., Leonard, N., Jones, S.L., Geurin, D., McKee, P.H., and Lawrence, C.M. (2004). Neonatal giant congenital nevi with proliferative nodules: a clinicopathologic study and literature review of neonatal melanoma. Arch. Dermatol. *140*, 83–88. https://doi.org/10.1001/archderm.140.1.83.

Love, M.I., Huber, W., and Anders, S. (2014). Moderated estimation of fold change and dispersion for RNA-seq data with DESeq2. Genome Biol *15*, 550. https://doi.org/10.1186/s13059-014-0550-8.

Martins da Silva, V., Martinez-Barrios, E., Tell-Martí, G., Dabad, M., Carrera, C., Aguilera, P., Brualla, D., Esteve-Codina, A., Vicente, A., Puig, S., et al. (2019). Genetic abnormalities in large to giant congenital nevi: Beyond NRAS mutations. J. Invest. Dermatol. *139*, 900–908. https://doi.org/10.1016/j.jid.2018.07.045.

Micali, G., Nasca, M.R., Tedeschi, A., Dall'Oglio, F., and Pulvirenti, N. (2000). Use of squaric acid dibutylester (SADBE) for cutaneous warts in children. Pediatr. Dermatol. *17*, 315–318. https://doi.org/10.1046/j.1525-1470.2000.01762.x.

Mir, A., Agim, N.G., Kane, A.A., Josephs, S.C., Park, J.Y., and Ludwig, K. (2019). Giant congenital melanocytic nevus treated With trametinib. Pediatrics *143*, e20182469. https://doi.org/10.1542/peds.2018-2469.

Newman, A.M., Liu, C.L., Green, M.R., Gentles, A.J., Feng, W., Xu, Y., Hoang, C.D., Diehn, M., and Alizadeh, A.A. (2015). Robust enumeration of cell subsets from tissue expression profiles. Nat. Methods *12*, 453–457. https://doi.org/10.1038/nmeth.3337.

Nishimura, E.K., Jordan, S.A., Oshima, H., Yoshida, H., Osawa, M., Moriyama, M., Jackson, I.J., Barrandon, Y., Miyachi, Y., and Nishikawa, S. (2002). Dominant role of the niche in melanocyte stem-cell fate determination. Nature *416*, 854–860. https://doi.org/10.1038/416854a.

Patro, R., Duggal, G., Love, M.I., Irizarry, R.A., and Kingsford, C. (2017). Salmon provides fast and bias-aware quantification of transcript expression. Nat. Methods *14*, 417–419. https://doi.org/10.1038/nmeth.4197.

Pawlikowski, J.S., Brock, C., Chen, S.C., Al-Olabi, L., Nixon, C., McGregor, F., Paine, S., Chanudet, E., Lambie, W., Holmes, W.M., et al. (2015). Acute inhibition of MEK suppresses congenital melanocytic nevus syndrome in a murine model driven by activated NRAS and Wnt signaling. J. Invest. Dermatol. *135*, 2902. https://doi.org/10.1038/jid.2015.230.

Pedersen, M., Küsters-Vandevelde, H.V.N., Viros, A., Groenen, P.J.T.A., Sanchez-Laorden, B., Gilhuis, J.H., van Engen-van Grunsven, I.A., Renier, W., Schieving, J., Niculescu-Duvaz, I., et al. (2013). Primary melanoma of the CNS in children is driven by congenital expression of oncogenic NRAS in melanocytes. Cancer Discov *3*, 458–469. https://doi.org/10.1158/2159-8290.CD-12-0464.

Phadke, P.A., Rakheja, D., Le, L.P., Selim, M.A., Kapur, P., Davis, A., Mihm, M.C., Jr., and Hoang, M.P. (2011). Proliferative nodules arising within congenital melanocytic nevi: a histologic, immunohistochemical, and molecular analyses of 43 cases. Am. J. Surg. Pathol. *35*, 656–669. https://doi.org/10.1097/PAS.0b013e31821375ea.

Price, H.N. (2016). Congenital melanocytic nevi: update in genetics and management. Curr. Opin. Pediatr. *28*, 476–482. https://doi.org/10.1097/MOP.0000000000000384.

Price, H.N., and Schaffer, J.V. (2010). Congenital melanocytic nevi-when to worry and how to treat: facts and controversies. Clin. Dermatol. *28*, 293–302. https://doi.org/10.1016/j.clindermatol.2010.04.004.

Qin, Q., Fan, J., Zheng, R., Wan, C., Mei, S., Wu, Q., Sun, H., Brown, M., Zhang, J., Meyer, C.A., and Liu, X.S. (2020). Lisa: inferring transcriptional regulators through integrative modeling of public chromatin accessibility and ChIP-seq data. Genome Biol *21*, 32. https://doi.org/10.1186/s13059-020-1934-6.

Riches, D.W., Chan, E.D., and Winston, B.W. (1996). TNF-alpha-induced regulation and signalling in macrophages. Immunobiology *195*, 477–490. https://doi.org/10.1016/s0171-2985(96)80017-9.

Rollins, B.J. (1991). JE/MCP-1: an early-response gene encodes a monocyte-specific cytokine. Cancer Cells *3*, 517–524.

Rouillé, T., Aractingi, S., Kadlub, N., Fraitag, S., How-Kit, A., Daunay, A., Hivelin, M., Moguelet, P., Picard, A., Fontaine, R.H., and Guégan, S. (2019). Local inhibition of MEK/Akt prevents cellular growth in human congenital melanocytic nevi. J. Invest. Dermatol. *139*, 2004–2015.e13. https://doi.org/10.1016/j.jid.2019.03.1156.

Sakai, K., Fukushima, S., Mizuhashi, S., Jinnin, M., Makino, T., Inoue, Y., and Ihn, H. (2020). Effect of topical immunotherapy with squaric acid dibutylester for alopecia areata in Japanese patients. Allergol. Int. *69*, 274–278. https://doi.org/10.1016/j.alit.2019.10.008.

Salim, T., Sershen, C.L., and May, E.E. (2016). Investigating the role of TNF-alpha and IFN-gamma activation on the dynamics of iNOS gene expression in LPS stimulated macrophages. PLoS One *11*, e0153289. https://doi.org/10.1371/journal.pone.0153289.

Schiferle, E.B., Cheon, S.Y., Ham, S., Son, H.G., Messerschmidt, J.L., Lawrence, D.P., Cohen, J.V., Flaherty, K.T., Moon, J.J., Lian, C.G., et al. (2021). Rejection of benign melanocytic nevi by nevus-resident $CD4^+$ T cells. Sci. Adv. *7*, eabg4498. https://doi.org/10.1126/sciadv.abg4498.

Schneider, C.A., Rasband, W.S., and Eliceiri, K.W. (2012). NIH Image to ImageJ: 25 years of image analysis. Nat. Methods *9*, 671–675. https://doi.org/10.1038/nmeth.2089.

Shah, K.N. (2010). The risk of melanoma and neurocutaneous melanosis associated with congenital melanocytic nevi. Semin. Cutan. Med. Surg. *29*, 159–164. https://doi.org/10.1016/j.sder.2010.06.007.

Shakhova, O., Zingg, D., Schaefer, S.M., Hari, L., Civenni, G., Blunschi, J., Claudinot, S., Okoniewski, M., Beermann, F., Mihic-Probst, D., et al. (2012). Sox10 promotes the formation and maintenance of giant congenital naevi and melanoma. Nat. Cell Biol. *14*, 882–890. https://doi.org/10.1038/ncb2535.

Silverberg, N.B., Lim, J.K., Paller, A.S., and Mancini, A.J. (2000). Squaric acid immunotherapy for warts in children. J. Am. Acad. Dermatol. *42*, 803–808. https://doi.org/10.1067/mjd.2000.103631.

Singh, M., Mansuri, M.S., Kadam, A., Palit, S.P., Dwivedi, M., Laddha, N.C., and Begum, R. (2021). Tumor necrosis factor-alpha affects melanocyte survival and melanin synthesis via multiple pathways in vitiligo. Cytokine *140*, 155432. https://doi.org/10.1016/j.cyto.2021.155432.

Tran, S.L., Haferkamp, S., Scurr, L.L., Gowrishankar, K., Becker, T.M., Desilva, C., Thompson, J.F., Scolyer, R.A., Kefford, R.F., and Rizos, H. (2012). Absence of distinguishing senescence traits in human melanocytic nevi. J. Invest. Dermatol. *132*, 2226–2234. https://doi.org/10.1038/jid.2012.126.

Tromberg, J., Bauer, B., Benvenuto-Andrade, C., and Marghoob, A.A. (2005). Congenital melanocytic nevi needing treatment. Dermatol. Ther. *18*, 136–150. https://doi.org/10.1111/j.1529-8019.2005.05012.x.

Tsao, A.S., Kantarjian, H., Cortes, J., O'Brien, S., and Talpaz, M. (2003). Imatinib mesylate causes hypopigmentation in the skin. Cancer *98*, 2483–2487. https://doi.org/10.1002/cncr.11812.

Valsecchi, R., Pansera, B., Rossi, A., and Cainelli, T. (1989). [Pigmentation abnormalities in the course of topical immunotherapy of alopecia areata]. G. Ital. Dermatol. Venereol. *124*, 31–32.

Viana, A.C., Gontijo, B., and Bittencourt, F.V. (2013). Giant congenital melanocytic nevus. An. Bras. Dermatol. *88*, 863–878. https://doi.org/10.1590/abd1806-4841.20132233.

Vocanson, M., Hennino, A., Rozières, A., Poyet, G., and Nicolas, J.F. (2009). Effector and regulatory mechanisms in allergic contact dermatitis. Allergy *64*, 1699–1714. https://doi.org/10.1111/j.1398-9995.2009.02082.x.

Vourc'h-Jourdain, M., Martin, L., Barbarot, S., and aRED.. (2013). Large congenital melanocytic nevi: therapeutic management and melanoma risk: a systematic review. J. Am. Acad. Dermatol. *68*, 493.e1. 498.e14. https://doi.org/10.1016/j.jaad.2012.09.039.

Wehrle-Haller, B. (2003). The role of Kit-ligand in melanocyte development and epidermal homeostasis. Pigment Cell Res. *16*, 287–296.

Wu, M., Hemesath, T.J., Takemoto, C.M., Horstmann, M.A., Wells, A.G., Price, E.R., Fisher, D.Z., and Fisher, D.E. (2000). c-kit triggers dual phosphorylations, which couple activation and degradation of the essential melanocyte factor Mi. Genes Dev. *14*, 301–312.

Xuan, W., Qu, Q., Zheng, B., Xiong, S., and Fan, G.H. (2015). The chemotaxis of M1 and M2 macrophages is regulated by different chemokines. J. Leukoc. Biol. *97*, 61–69. https://doi.org/10.1189/jlb.1A0314-170R.

Yang, X., Liang, R., Liu, C., Liu, J.A., Cheung, M.P.L., Liu, X., Man, O.Y., Guan, X.Y., Lung, H.L., and Cheung, M. (2019). SOX9 is a dose-dependent metastatic fate determinant in melanoma. J. Exp. Clin. Cancer Res. *38*, 17. https://doi.org/10.1186/s13046-018-0998-6.

Yoshida, H., Kunisada, T., Grimm, T., Nishimura, E.K., Nishioka, E., and Nishikawa, S.I. (2001). Review: melanocyte migration and survival controlled by SCF/c-kit expression. J. Investig. Dermatol. Symp. Proc. *6*, 1–5. https://doi.org/10.1046/j.0022-202x.2001.00006.x.

Yu, G., Wang, L.G., Han, Y., and He, Q.Y. (2012). clusterProfiler: an R package for comparing biological themes among gene clusters. Omics *16*, 284–287. https://doi.org/10.1089/omi.2011.0118.

Zaal, L.H., Mooi, W.J., Klip, H., and van der Horst, C.M. (2005). Risk of malignant transformation of congenital melanocytic nevi: a retrospective nationwide study from the Netherlands. Plast. Reconstr. Surg. *116*, 1902–1909. https://doi.org/10.1097/01.prs.0000189205.85968.12.

Zöller, M., Freyschmidt-Paul, P., Vitacolonna, M., McElwee, K.J., Hummel, S., and Hoffmann, R. (2004). Chronic delayed-type hypersensitivity reaction as a means to treat alopecia areata. Clin. Exp. Immunol. *135*, 398–408. https://doi.org/10.1111/j.1365-2249.2003.02380.x.

STAR★METHODS

KEY RESOURCES TABLE

REAGENT or RESOURCE	SOURCE	IDENTIFIER
Antibodies		
Mouse monoclonal anti-TRP2/DCT	Santa Cruz Biotechnology	Cat#sc-74439; RRID:AB_1130818
Mouse monoclonal anti-SOX10	Santa Cruz Biotechnology	Cat# sc-365692; RRID:AB_10844002
Mouse monoclonal anti-MITF	Leica Biosystems	Cat# NCL-L-MITF; RRID:AB_564111
Mouse monoclonal anti-Ki67	Leica Biosystems	Cat# KI67-MM1-CE; RRID:AB_563841
Rabbit polyclonal anti-S100	DAKO	Cat# Z031129-2; RRID:AB_2315306
Mouse monoclonal anti-HMB45	DAKO	Cat# M0634; RRID:AB_2335682
Rabbit monoclonal anti-Phospho-p44/42 MAPK	Cell Signaling Technology	Cat# 4370; RRID:AB_2315112
Rabbit monoclonal anti-Phospho-MEK1/2 (Ser221) (166F8)	Cell Signaling Technology	Cat# 2338; RRID:AB_490903
Mouse monoclonal anti-PCNA	Cell Signaling Technology	Cat# 2586; RRID:AB_2160343
Rabbit monoclonal anti-CD8	Cell Signaling Technology	Cat# 98941; RRID:AB_2756376
Rabbit polyclonal anti-CD163	Biorbyt	Cat# orb13303; RRID:AB_10749283
Mouse monoclonal anti-CD161	Novus Biologicals	Cat# NBP2-14844; RRID: N/A
Rabbit polyclonal anti-NRAS^{Q61R}	Abcam	Cat# ab227658; RRID: N/A
Mouse monoclonal anti-p16^{INK4A}	Abcam	Cat# ab54210; RRID:AB_881819
Rabbit monoclonal anti-MelanA	Abcam	Cat #ab210546; RRID:AB_2889292
Hamster monoclonal anti-CD11c	Abcam	Cat# ab33483; RRID:AB_726084
Rat monoclonal anti-CD3	Abcam	Cat# ab11089; RRID:AB_2889189
Rabbit monoclonal anti-CD4	Abcam	Cat# ab183685; RRID:AB_2686917
Rat monoclonal InVivoMAb anti-mouse CD4	BioXCell	Cat# BE0003-1; RRID:AB_1107636
Rat monoclonal InVivoMAb anti-mouse CD8α	BioXCell	Cat# BE0061; RRID:AB_1125541
Rat monoclonal InVivoMAb rat IgG2b isotype control, anti-keyhole limpet hemocyanin	BioXCell	Cat# BE0090; RRID:AB_1107780
Rat monoclonal InVivoMab anti-mouse F4/80	BioXCell	Cat# BE0206; RRID:AB_10949019
Rabbit polyclonal anti-TRP2	Abcam	Cat# ab74073; RRID:AB_1524517
Rat monoclonal anti-F4/80	Abcam	Cat# ab16911; RRID:AB_443548
Goat polyclonal Alexa Fluor 488-AffiniPure Anti-Rabbit IgG (H+L)	Jackson ImmunoResearch Labs	Cat# 111-545-144; RRID:AB_2338052
Donkey polyclonal Alexa Fluor® 594 AffiniPure Anti-Rabbit IgG (H+L)	Jackson ImmunoResearch Labs	Cat# 711-585-152; RRID:AB_2340621
Rabbit monoclonal anti-SOX10	Abcam	Cat# ab155279; RRID:AB_2650603
Mouse monoclonal anti-HMB-45	Abcam	Cat# ab732; RRID:AB_305844
Biological samples		
De-identified nevus tissue	Mass General Brigham Healthcare	IRB Protocol 2017P000992
Chemicals, peptides, and recombinant proteins		
4-hydroxytamoxifen	Sigma-Aldrich	Cat#H6278; CAS: 68392-35-8
Binimetinib (MEK162)	Selleckchem	Cat#S7007; CAS 606143-89-9
Trametinib (GSK1120212)	Selleckchem	Cat# S2673; CAS 871700-17-3
Omipalisib (GSK2126458)	Selleckchem	Cat# S2658; CAS 1086062-66-9
Imatinib (STI571)	Selleckchem	Cat# S2475; CAS 152459-95-5
Squaric acid dibutylester (SADBE)	Sigma-Aldrich	Cat# 339792; CAS 2892-62-8
16% Paraformaldehyde Aqueous Solution, EM Grade, Ampoule 10 ML	Electron Microscopy Sciences	Cat# 50-980-487

(*Continued on next page*)

Continued

REAGENT or RESOURCE	SOURCE	IDENTIFIER
Hematoxylin 2	Epredia	Cat# 7231
Nuclear Fast Red	Abcam	Cat #ab246831
RNAlater	Life Technologies	Cat# AM7020
EQUISUL-SDT® (SULFADIAZINE/TRIMETHOPRIM)	Aurora Pharmaceuticals	Cat# SC-395895Rx
Citrate Buffer (pH 6.0), Concentrate	Life Technologies	Cat# 005000
Goat Serum	Sigma Aldrich	Cat# G9023
DAPI	Sigma Aldrich	Cat# D9542; CAS:28718-90-3
Fluoromount G	Southern Biotech	Cat# 0100-01
Critical commercial assays		
RNeasy Plus Universal Kit	Qiagen	Cat# 73404
Agilent RNA 6000 Nano Kit	Agilent Technologies	Cat# G2938-90034
Fontana-Masson Stain Kit (Melanin Stain)	Abcam	Cat# ab150669
RNA FFPE Miniprep kit	Zymo Research	Cat# R1009
Agilent RNA 6000 Pico Kit	Agilent Technologies	Cat# G2938-90046
Quant-it™ RiboGreen RNA Assay Kit and RiboGreen RNA Reagent	ThermoFisher Scientific	Cat# R11490
Illumina Ribo-Zero Plus rRNA Depletion Kit	Illumina	Cat# 20037135
QIAamp DNA FFPE Tissue Kit	Qiagen	Cat# 56404
High Sensitivity RNA ScreenTape Analysis	Agilent Technologies	Cat# 5067-5579
Illumina® Stranded mRNA Prep, Ligation (96 Samples)	Ilumina	Cat# 20040534
Deposited data		
Raw and analyzed CMN Model RNA Seq Data	This Paper	GEO: GSE199891; GEO: GSE199894
Raw and analyzed DCT SADBE RNA Seq Data	This Paper	GEO: GSE199893
LM22 (leukocyte gene signature matrix)	Stanford University CIBERSORT	Newman et al. 2015
Experimental models: Organisms/strains		
Mouse: Lox-stop-Lox (LSL)-*Nras*^{Q61R}: *C57Bl/6 Nras*$^{tm1.1Nesh}$	Burd et al., 2014 Sourced from Drs. Christin Burd and Norman Sharpless, University of North Carolina	MGI:5645358
Mouse: *Dct*-Cre: C57BL/6 *Dct*$^{tm1(Cre)Bee}$	Guyonneau et al., 2004 Sourced from Dr. Friedrich Beermann, ISREC, Lausanne, Switzerland	MGI:2387116
Mouse: *Tyr*-Cre: C57BL/6 Tg(Tyr-cre)1Lru	Delmas et al., 2003 Source from Dr. Lionel Larue, Institut Curie, Paris, France	MGI:3573939
Mouse: *Tyr*-CreER^{T2}: C57Bl/6 Tg(Tyr-cre/ERT2)13Bos	Bosenberg et al., 2006 Sourced from Dr. Marcus Bosenberg, Yale University	MGI:3641203
Mouse:SHO: Crl:SHO-*Prkdc*^{scid}*Hr*^{hr}	Charles River Laboratories	RRID: IMSR_CRL:474
Oligonucleotides		
Primer DCT Forward: TTGAGAGGAGAGG AAAGGGC	Guyonneau et al., 2004	N/A
Primer DCT Reverse: CACGCCATCCAA GGTCATGC	Guyonneau et al., 2004	N/A
Primer CRE Reverse: CATTGCTGTCACT TGGTCGT	Guyonneau et al., 2004	N/A
Primer NRAS Q61R: GCAAGAGGCCCGG CAGTACCTA	Burd et al., 2014	N/A

(*Continued on next page*)

Continued

REAGENT or RESOURCE	SOURCE	IDENTIFIER
Primer NRAS 1: AGACGCGGAGACTTGG CGAGC	Burd et al., 2014	N/A
Primer NRAS 2: GCTGGATCGTCAAGG CGCTTTTCC	Burd et al., 2014	N/A
Primer Tyr::CRE<ERT2> 1: CAGGGTGTTATA AGCAATCCC	Bosenberg et al., 2006	N/A
Primer Tyr::CRE<ERT2> 2: CCTGGAAAATGC TTCTGTCCG	Bosenberg et al., 2006	N/A
Primer Tyr::CRE Forward: GTCACTCCAGGG GTTGCTGG	Delmas et al., 2003	N/A
Primer Tyr::CRE Reverse: CCGCCGCATAA CCAGTGA	Delmas et al., 2003	N/A
Software and algorithms		
GraphPad Random Treatment Assigner	GraphPad	https://www.graphpad.com/quickcalcs/randomize1/
Zeiss Zen Image Software, Version 2.3	Zeiss	https://www.zeiss.com/microscopy/us/products/microscope-software/zen.html
ImageJ	National Institutes of Health (NIH)	https://imagej.nih.gov/ij/
NIS Elements imaging software	Nikon Instruments Inc	www.microscope.healthcare.nikon.com/products/software/nis-elements
DESeq2	Bioconductor	https://bioconductor.org/packages/release/bioc/html/DESeq2.html
Prism 7	Graphpad	https://www.graphpad.com/support/prism-7-updates/
DRAGEN FastQC	Illumina	https://support.illumina.com/content/dam/illumina-support/help/Illumina_DRAGEN_Bio_IT_Platform_v3_7_1000000141465/Content/SW/Informatics/Dragen/FASTQC_Intro_fDG.htm
Salmon v 1.8.0	Patro et al., 2017	https://github.com/COMBINE-lab/Salmon
NDP.view2 v 2.8.24	Hamamatsu	https://www.hamamatsu.com/us/en/product/life-science-and-medical-systems/digital-slide-scanner/U12388-01.html
R package: fgsea	Korotkevich et al., 2021	https://doi.org/10.1101/060012
R package: clusterProfiler	Yu et al., 2012	https://doi.org/10.1089/omi.2011.0118

RESOURCE AVAILABILITY

Lead contact

Further information and requests for resources and reagents should be directed to and will be fulfilled by the lead contact Dr. David Fisher, M.D., Ph.D. (DFISHER3@mgh.harvard.edu).

Materials availability

Mouse lines generated in this study will be distributed upon request to other investigators under a Material Transfer Agreement. All unique/stable reagents generated in this study are available from the lead contact with a completed Materials Transfer Agreement.

Data and code availability

All the Software packages and methods used in this study have been properly detailed and referenced under the Software and algorithms listed in key resources table. All RNA-seq data has been deposited at GEO and are publicly available as of the date of publication. Accession numbers are listed in the key resources table. This paper does not report original code. Any additional information required to reanalyze the data reported in this paper is available from the lead contact upon request.

EXPERIMENTAL MODEL AND SUBJECT DETAILS

Ethics Statement

Mouse studies and procedures were approved by the Institutional Animal Care and Use Committee of Massachusetts General Hospital and conducted strictly in accordance with the approved animal handling protocol.

Mice

Mice were assigned randomly to the different experimental groups by covariate adaptive randomization using an online calculator (www.graphpad.com/quickcalcs/randomize1/). All mice were matched by gender and age, as indicated in each experiment. All mice were group-housed, fed ProLab IsoPro RMH 300 Irradiated feed, and kept at 68-73 °F. Mice were genotyped according to the protocol obtained from their respective publications or distributers. Primers can be found in the key resources table.

Generation of melanocyte-specific $Nras^{Q61R}$ *mutant mice*

Melanocyte-specific $Nras^{Q61R}$ expression was induced by crossing LSL-$Nras^{Q61R}$ mice (Burd et al., 2014) (generated by Drs. Christin Burd and Norman Sharpless, University of North Carolina) with melanocyte-targeted Cre recombinase transgenic mice containing either *Dct* promoter-driven Cre (*Dct*-Cre mice (Guyonneau et al., 2004), kindly provided by Dr. Friedrich Beermann, ISREC, Lausanne, Switzerland), *Tyr* promoter-driven Cre *Tyr*-Cre mice (Delmas et al., 2003), kindly provided by Dr. Lionel Larue, Institut Curie, Paris, France), or inducible *Tyr* promoter-driven $CreER^{T2}$ (*Tyr*-$CreER^{T2}$ mice) (Bosenberg et al., 2006), kindly provided by Dr. Marcus Bosenberg, Yale University). To obtain a melanocyte-specific inducible *Nras* mutation, two-day- old female LSL-$Nras^{Q61R}$ newborn mice harboring *Tyr*-$CreER^{T2}$ were painted topically with 25 mg/ml 4-hydroxytamoxifen (Sigma-Aldrich, #H6278) dissolved in dimethyl sulfoxide (DMSO), once daily for 1 week.

METHOD DETAILS

Animal studies and analysis of melanoma incidence

We measured the incidence of $Nras^{Q61R}$ mutation-driven melanoma formation in both *Dct*-Cre $Nras^{Q61R}$ mutant and tamoxifen-induced *Tyr*-$CreER^{T2}$ $Nras^{Q61R}$ mutant mice. These experiments were performed with > 20 mice per group (both genders, classified by ages), and their survival curves were calculated by the log-rank test at a two-sided significance level of $P<0.05$.

Quantification of proliferative and senescent phases

Dorsal skin samples from *Dct*-Cre $Nras^{Q61R/Q61R}$ mutant mice were harvested at the ages indicated. Samples from three mice of each age group, with five to ten nonadjacent samples per mouse, were quantified. Nevus cell proliferation and senescence were measured by immunofluorescence staining for Ki67 (Leica Biosystems, #KI67-MM1-CE) and $p16^{Ink4a}$ (Abcam, # ab54210), respectively and quantification of Ki67+MelanA+ double-positive proliferative nevus cells or p16+MelanA+ double-positive senescent nevus cells was calculated as a percentage of the total number of MelanA+ positive nevus cells.

Quantification of Melan A or iNOS positive cells

Ear skin samples from three mice of each study group, with three to five non-adjacent samples per mouse, were quantified. The number of MelanA-positive nevus cells (Figure 6A) or iNOS-positive cells (Figure 6B) was measured and calculated per mm^2 unit area.

Treatment procedures for therapeutic agents

Selected therapeutic agents or vehicle controls were applied on $Nras^{Q61R}$ mutation-driven nevus lesions by either direct intralesional injection (paws) or topical application (ears and dorsal skin). Agents tested included: (1) small molecules targeting NRAS signaling pathways: binimetinib (MEK162) (Sellechkchem, #S7007), trametinib (GSK1120212) (Selleckchem, #S2673), and omipalisib (GSK2126458) (Selleckchem, #S2658); (2) the melanocyte-selective toxic agent, imatinib (STI571) (Selleckchem, #S2475); SADBE (squaric acid dibutylester) (Sigma-Aldrich, #339792). Details are provided in Table S1 For all topical hapten-based immunotherapies. Mice were sensitized with 2% SADBE in acetone which was applied to the right side of the shaved abdomen. Three days later, sensitized mice were challenged with the same drug applied to the right ear or dorsal skin. An identical quantity of acetone (without SADBE) was administered topically to the left ear or dorsal skin as control. All drug treatments in mice were performed under isoflurane inhalation anesthesia. Mice were examined for signs of toxicity and for depigmentation during each treatment. Animals were euthanized in accordance with a set schedule, and the treated lesions were collected and processed for assessment of melanocyte destruction. Each sample was compared to the vehicle control from the same mouse, and five mice per treatment group were typically used excluding 0.5% SADBE 3 times per week for 2 weeks, where 3 mice per treatment group were used (Figure S4B).

Histology, staining, and imaging

Skin samples were taken from euthanized mice, fixed in 4% paraformaldehyde (Electron Microscopy Sciences, #50-980-487) overnight at 4°C, and embedded in paraffin using standard procedures. 5 μm sections were prepared from tissue blocks and stained with hematoxylin and eosin (H&E) (Epredia, #7231) for histologic analysis. Fontana-Masson silver stain (Abcam, #ab150669) was used to detect the melanin pigments following the provided protocol with one modification by leaving the slides in Ammoniacal Silver solution

for 40 minutes rather than the recommended 30 minutes for melanin, and stained sections were counterstained with Nuclear Fast Red (Abcam, #ab246831). Stained images were captured using a Hamamatsu Nanozoomer, and analyzed using NDP.view2 software (Hamamatsu).

For immunostaining, sections were subjected to heat-induced antigen retrieval and incubated with primary antibodies against TRP2/DCT (1:100) or SOX10 (1:50) (Santa Cruz Biotechnology, #sc-74439, #sc-365692); MITF (1:50) or Ki67 (1:50) (Leica Biosystems, #NCL-L-MITF, #KI67-MM1-CE); S100 (1:2000) or HMB-45 (1:100) (DAKO, #Z031129-2, #M0634); p-p44/42 MAPK (1:50), p-MEK1/2 (1:50), PCNA (1:2000), or CD8 (1:400) (Cell Signaling Technology, #4370, #2338, #2586); CD163 (1:100) (Biorbyt, #orb13303); CD161 (1:50) (Novus Biologicals, #NBP2-14844); NRASQ61R (1:100), p16INK4A (1:1000), MelanA (1:500), CD11c (1:100), CD3 (1:100), or CD4 (1:500) (Abcam, #ab227658, #ab54210, #ab210546, #ab33483, #ab33483, #ab11089, #ab183685). Stained images were captured using a Zeiss AxioObserver Z1 microscope and an AxioCam MRC digital camera for brightfield or Photometrics CoolSNAP HQ2 interline CCD camera for fluorescence, and Ziess Zen software, version 2.3 (Carl Zeiss Microscopy LLC, Thornwood, NY, USA). Immunofluorescence-stained sections were counterstained with 4',6-diamidino-2-phenylindole (DAPI) (Sigma Aldrich, #D9542), and ImageJ software (National Institutes of Health [NIH]) (Schneider et al., 2012) was used for image processing and analysis. Skin tissue images were obtained with a Nikon SMZ1500 stereomicroscope, a Nikon DS-Ri2 microscope camera, and NIS Elements imaging software, version 4.30 (Nikon Instruments Inc., Melville, NY, USA).

Nras loss of heterozygosity

DNA from 5-10 5um sections taken from paraffin blocks, was extracted using the QIAamp DNA FFPE Tissue Kit (QIAGEN, #56404). PCR reactions were run with approximately 200ng of DNA following the established genotyping test PCR for the *Dct*:CRE, *Nras* mice. PCR products were run on a QIAxcel to visualize the bands and determine estimated concentrations. Toe DNA samples were collected during routine genotyping of pups to use as controls.

In vivo depletion of immune cells

750 μg of the following antibodies were IP injected on day 7, 4, and 2 prior to sensitization with SADBE, and 300 μg on days 0 (sensitization with 2% SADBE), 3, 5, 7, 10: InVivoMAb anti-mouse CD4_GK1.5 clone (BioXCell, #BE0003-1), InVivoMAb anti-mouse CD8α _2.43 clone (BioXCell, #BE0061), InVivoMAb anti-rat IgG2b isotype control; anti-keyhole limpet hemocyanin_LTF-2 clone (BioXCell, #BE0090), and InVivoMAb anti-mouse F4/80_CI:A3-1 clone (BioXCell, #BE0206).

RNA-Sequencing of SADBE treated samples

Whole skin sections were harvested from treated areas of *Dct*-Cre $Nras^{Q61R/+}$ mice 72 hours after treatment with 2% SADBE or vehicle control (acetone) and stored in RNAlater (Ambion/Life Technologies, #AM7020). Total RNA was isolated from skin using the RNeasy Plus Universal Kit (Qiagen, #73404) with disruption and homogenization using the TissueLyser II system (Qiagen). All extracted RNA samples possessed RIN > 8.0 by Agilent TapeStation System with High Sensitivity RNA Screen Tape (Agilent Technologies, #5067-55779) and proceeded for NGS library construction with Illumina Stranded mRNA Prep, Ligation kit (Illumina, #20040534). Each amplified, then bead-cleaned library was assessed for its quality and quantity by Agilent TapeStation with High Sensitivity D1000 ScreenTape and Qubit fluorometer 4.0.(Invitrogen), respectively. Each library was normalized at 4 nM, then pooled, denatured, and loaded onto the Illumina NextSeq550 at 2x74 base-pair specification. The generated FastQ files were processed under DRAGEN FastQC bioinformatic pipeline (Illumina) to assess the overall quality of the data for adapter contamination or GC content.

RNA-Sequencing mouse model comparison

FFPE blocks of tumor and control tissues(n=18) were cut at 8 um thickness and RNA was extracted with RNA FFPE Miniprep kit (Zymo Research, #R1009) following manufacturer recommendations. Extracted RNA quality was assessed by the Agilent Bioanalyzer system with Eukaryote Total RNA Pico assay (Agilent Technologies, #G2938-90046). The overall quantity was measured by Nanodrop 2000 Spectrophotometer followed by Quant-it RiboGreen RNA Assay (ThermoFisher Scientific, #R11490) to optimize inputs for NGS library construction. The maximum input of 1 ug was processed for library construction with Stranded total RNA with ligation with Ribozero plus kit (Illumina, #20037135). Each amplified then bead-cleaned library was assessed for its quality and quantity by Agilent TapeStation with High Sensitivity D1000 ScreenTapes and Qubit fluorometer 4.0. (Invitrogen, Waltham, MA), respectively. Each library was normalized at 4 nM, then pooled, denatured, and loaded onto the Illumina NextSeq550 targeting 80 million reads per sample at 1x76 base-pair specification. The generated FastQ files were processed under DRAGEN FastQC bioinformatic pipeline (Illumina) to assess the overall quality of the data for adapter contamination or GC content.

RNA-Sequencing Analysis

We performed RNA-seq and differential expression analysis for in-house mouse RNA-seq datasets and one publicly available human nevi cohort. Read alignment was preformed using STAR (Dobin et al., 2013), followed by transcript quantification using Salmon (Patro et al., 2017), and differential analysis using DESeq2(Love et al., 2014) that compares SADBE-treated samples and control samples. The set of differentially expressed genes were determined using absolute LogFoldChange>1 and FDR<0.01. To investigate macrophage-related genes, we obtained macrophage gene lists from LM22 (Newman et al., 2015) which includes markers for macrophage

states M0, M1, and M2. We also obtained from TIDE (Jiang et al., 2018) the gene correlation scores with tumor M2 macrophage levels. For the systematic (Jiang et al., 2018) pathway analysis on differentially expressed genes, we performed gene-set enrichment analysis using R packages fgsea(Korotkevich et al., 2021) and clusterProfiler(Yu et al., 2012). The above analysis was performed on both mouse and human RNA-seq datasets using corresponding genomic references in each species; specifically, for the mouse set with untreated nevi, normal, and melanoma, differential expression was carried out using protein-coding genes to facilitate pathway interpretation between nevi and normal skin samples. After obtaining differential gene lists, we applied LISA (Qin et al., 2020) to infer transcriptional regulators using public ChIP-seq profiles.

Transplantation of CMN xenografts

Discarded de-identified nevus tissue was obtained under IRB approved protocol 2017P000992 (Mass General Brigham Healthcare). Nevi were transplanted onto the back of SHO (Charles River Laboratories, MA, USA) 62-day-old female mice according to previous published work (Schiferle et al., 2021). Briefly, using a DermaBlade Shave Biopsy Instrument (AccuTec Blades Inc., #72-0001-0000) under sterile conditions, subcutaneous dermal fat was removed from the dermal side of the giant nevus to enhance vascularization and grafting efficiency. Mice were anesthetized and placed on a heating pad. The surgical site was sterilized with 70% ethanol. Nevi were transplanted onto recipient mice using surgical grade sutures and were bandaged using Vaseline gauze and elastic adhesive bandage. Mice were placed on sulfadiazine/trimethoprim antibiotics (Equisul-SDT Oral Suspension) (Aurora Pharmaceuticals, #sc-395895Rx) after transplantation. Bandages were removed 5 to 7 days after surgery and graft sutures were removed 14 days post-surgery.

SADBE treatment of xenografts

8 xenografts from one donor were implanted on 4 SHO 62-day-old female mice and 2 xenografts from an additional donor were implanted on 1 SHO mouse. For melanocyte cell count, topical application of 1% SADBE using a cotton tip was performed twice a week for 8 months on 3 of the xenografts, 5 of the xenografts from the same donor received acetone control. Treatments did not induce recognized side effects; behavior remained normal and morphologic structure of the skin remained intact with minimal surrounding erythema. For macrophage cell counts, 2 additional xenografts from a different donor were treated with 1% SADBE or acetone control for 2 weeks after which the xenografts were harvested for further F4/80 macrophage staining.

Imaging of CMN xenografts

Formalin–fixed paraffin-embedded CMN xenografts (5 μm) were labeled with the following antibodies: TRP2 antibody (1:100) (Abcam, #ab74073) and F4/80 antibody (1:100) (Abcam, #ab16911). Deparaffinization of slides was performed with 100% xylene for 2x5 min, followed by 100, 90, 70, 50 and 30% ethanol for 2 min each. Slides were washed in PBS for 5 min. Permeabilization was conducted in 0.2% triton-X for 5 min and then the slides were washed 2x3 min in 0.01% PBS-tween 20. Antigen retrieval was performed by incubating the slides with citrate buffer (pH = 6) at 95 °C for 20 minutes. Sections were washed with 0.01% PBS-tween 20 for 3x3 min and blocked for 1 hour with PBS containing 10% normal goat serum and 5% BSA. Slides were incubated overnight at 4 °C with primary antibodies diluted in blocking buffer. Sections were washed with 0.01% PBS-tween 20 for 3x3 min, followed by secondary antibody incubation [1:500; goat anti-Rabbit IgG (H+L) Alexa Fluor® 488-AffiniPure (Jackson ImmunoResearch Laboratories, #111-545-144), or 1:500 Alexa Fluor® 594 AffiniPure Donkey Anti-Rabbit IgG (H+L) (Jackson ImmunoResearch Laboratories, #711-585-152)] for 2 hours at room temperature. Slides were washed 3x3 min with 0.01% PBS-tween 20, incubated with DAPI (Sigma-Aldrich, #D9542) for 5 minutes for nuclei staining and coverslipped using Fluoromount G (Southern Biotech, #0100-01). Slides were placed at 4 °C for 48 hours before imaging.

Photomicrographs were obtained under either×20 or×40 objective using a Ziess Axio Photo Observer Microscope or Nikon SMZ1500 stereomicroscope. ImageJ (National Institutes of Health [NIH]) was used to identify cells based on size, circularity, nuclear presence, and intensity. Positive cells were counted in both the epidermis and dermis of each specimen for F4/80 and throughout epidermis for TRP2. In each area, the number of positive cells was counted and reported in relationship to the total number of DAPI-positive cells. Thus, results are expressed as a percentage of positive cells for each marker analyzed per total cells. Quantifications were done on multiple sections from each CMN xenograft, typically 3-20 images per sample.

QUANTIFICATION AND STATISTICAL ANALYSIS

All statistical analyses were performed with GraphPad Prism 7 software, and the evaluations were conducted by using a Student's t-test, one-way ANOVA with Tukey's multiple comparison test, or log-rank test for survival analysis. A probability value of $P<0.05$ was considered statistically significant (*$P<0.05$; **$P<0.01$; ***$P<0.001$; ****$P<0.0001$).

Supplemental figures

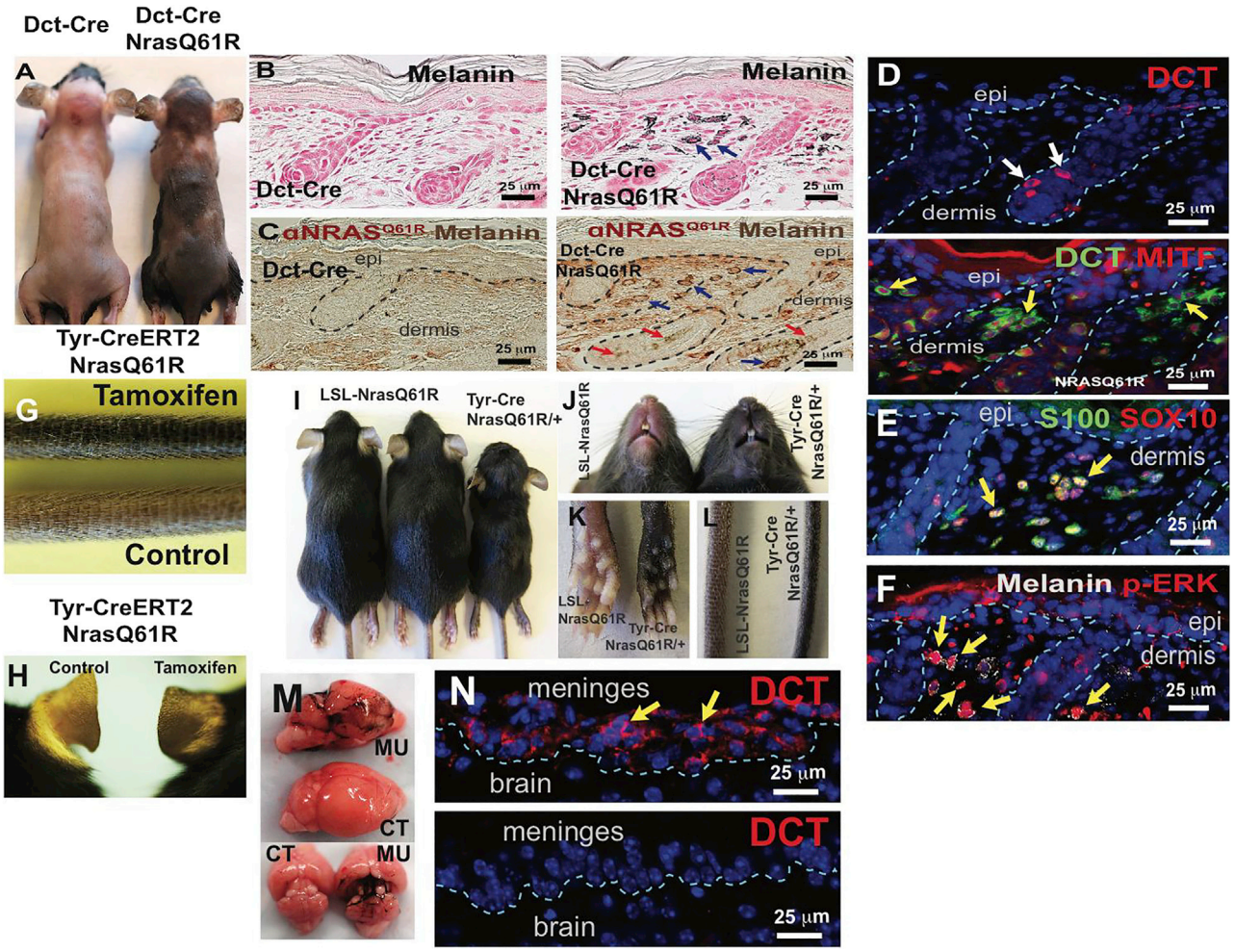

Figure S1. Additional melanocyte-specific *Nras*^{Q61R} mutation-driven congenital nevus models mimic genetic and phenotypic features of human giant congenital nevi, related to Figure 1

(A–F) (A) Features of melanocytic nevi of adult *Dct*-Cre *Nras*^{Q61R} mouse. (B–F) Features of melanocytic nevi of 3-day-old *Dct*-Cre *Nras*^{Q61R} mouse. (A) Skin hyperpigmentation was observed in melanocyte-specific *Nras*^{Q61R} mutant mice, but not in control mice. (B) Melanin from 3-day-old *Dct*-Cre *Nras*^{Q61R} mice was detected by Fontana-Masson staining. (C–F) Immunostaining of paraffin sections. Paraffin sections were immunostained for (mutant-specific) *Nras*^{Q61R} (C, dark brown), DCT (D, red in upper panel, green in lower panel), MITF (D, red in lower panel), S100 (E, green), SOX10 (E, red), or p-ERK (F, red). Red arrows in (C) indicate follicular melanin detected by bright-field microscopy, blue arrows in (C) indicate positive signals. Phosphorylated ERK (yellow arrows in F) was detectable in dermal nevus cells showing melanin deposition (white, F).

(G and H) Features of melanocytic nevi of tamoxifen-induced *Tyr*-CreER^{T2} *Nras*^{Q61R} mutant mice were observed (G, tail, H, ear).

(I) Surviving *Tyr*-Cre *Nras*$^{Q61R/+}$ heterozygous mutant mouse was compared with control littermates at 1 month of age. The mutant mouse developed hydrocephalus and had growth retardation.

(J–L) Hyperpigmentation. Skin hyperpigmentation in *Tyr*-Cre *Nras*$^{Q61R/+}$ mice was observed in the snout/perioral region (J), paws (K), and tail (L).

(M and N) Ectopic pigmentation was compared in the parietal-temporal lobe (M, upper image) and the area of the superior and interior colliculi (N, lower image). Yellow arrows in (N) indicate ectopic melanocytes in the meninges of the mutant brain, but not in control tissue.

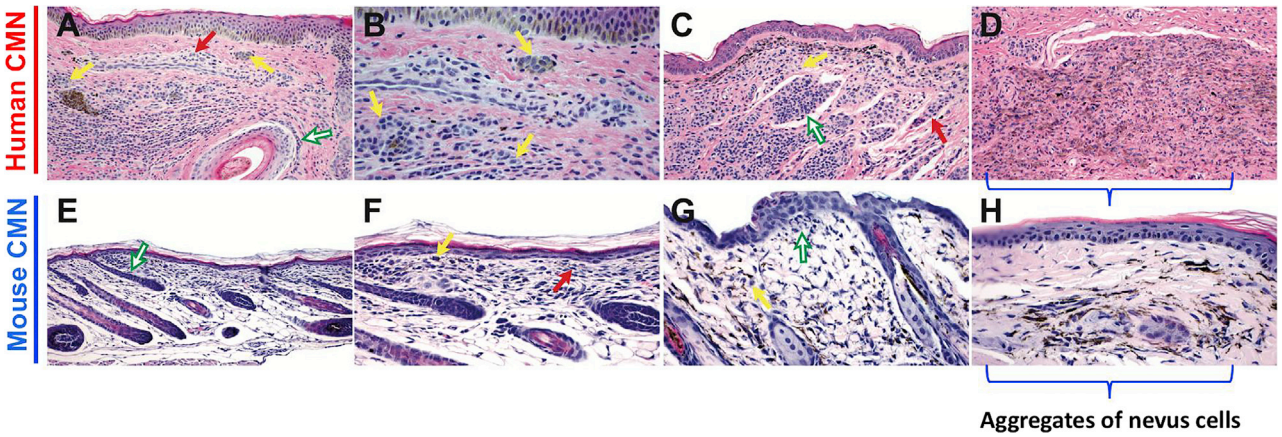

Figure S2. Comparison of mouse vs human giant congenital nevi, related to Figure 1

(A–D) hematoxylin and eosin (H&E) stained histological images of human congenital nevi.

(E–H) hematoxylin and eosin (H&E) stained histological images of *Nras*^{Q61R} mutation-driven murine congenital nevi. Histologic images at low magnifications (A, C, and D, 200×) and high magnification (B, E, G, and H, 400×; F: 600×) are presented. Yellow arrows in (A) indicate nevus cells. Red arrow in (A) indicates nevi exhibiting perivascular distribution. Green arrow (A) indicates nevi associated with the adventitia of the hair follicle. Yellow arrows in (B) indicate nevus cells having hyperchromatic nuclei. Green arrow in (E) indicates nevus cells distributed around some adnexal structures. Yellow arrow in (F) indicates nevus cells with small hyperchromatic nuclei. Red arrow in (F) indicates spindle-shaped nevus cells. Yellow arrow in (C) indicates nevus cells displaying increased cytoplasm. Green arrow in (C) indicates large nests of pigmentation. Red arrow in (C) indicates melanocytes infiltrating the reticular dermis. Yellow arrow in (G) indicates nevus cells having hyperchromatic nuclei and a round cytoplasm. Green arrow in (G) indicates a superficial aggregate of nevus cells forming a nest.

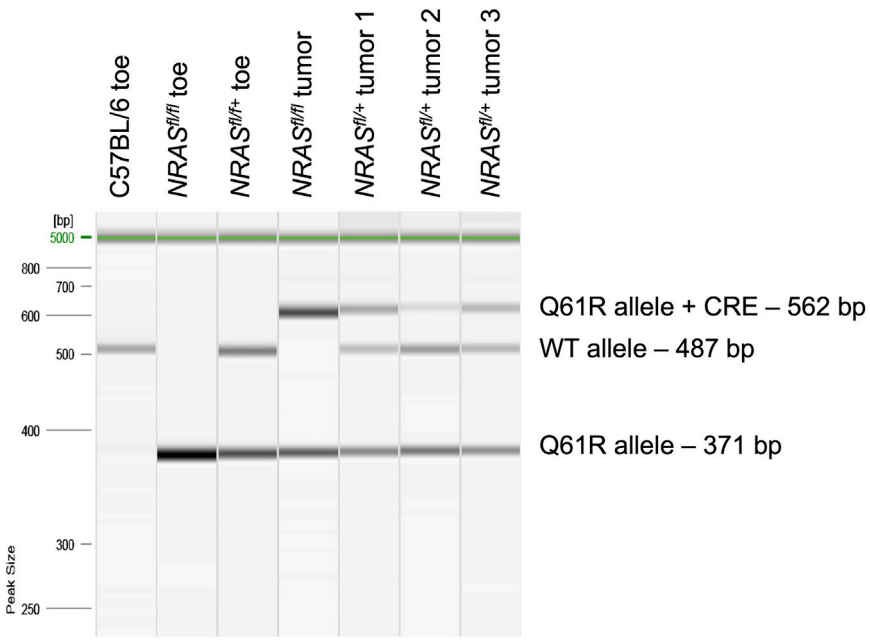

Figure S3. Loss of heterozygosity determination in *Nras*-driven mice melanoma, related to Figure 3

3 heterozygous *Dct*-Cre *Nras*$^{Q61R/+}$ tumors and control tissue were tested using PCR primers that discriminate between the wild-type (WT), mutant (Q61R), and recombined mutant (Q61R+CRE) alleles. All three tumors retained the wild-type allele.

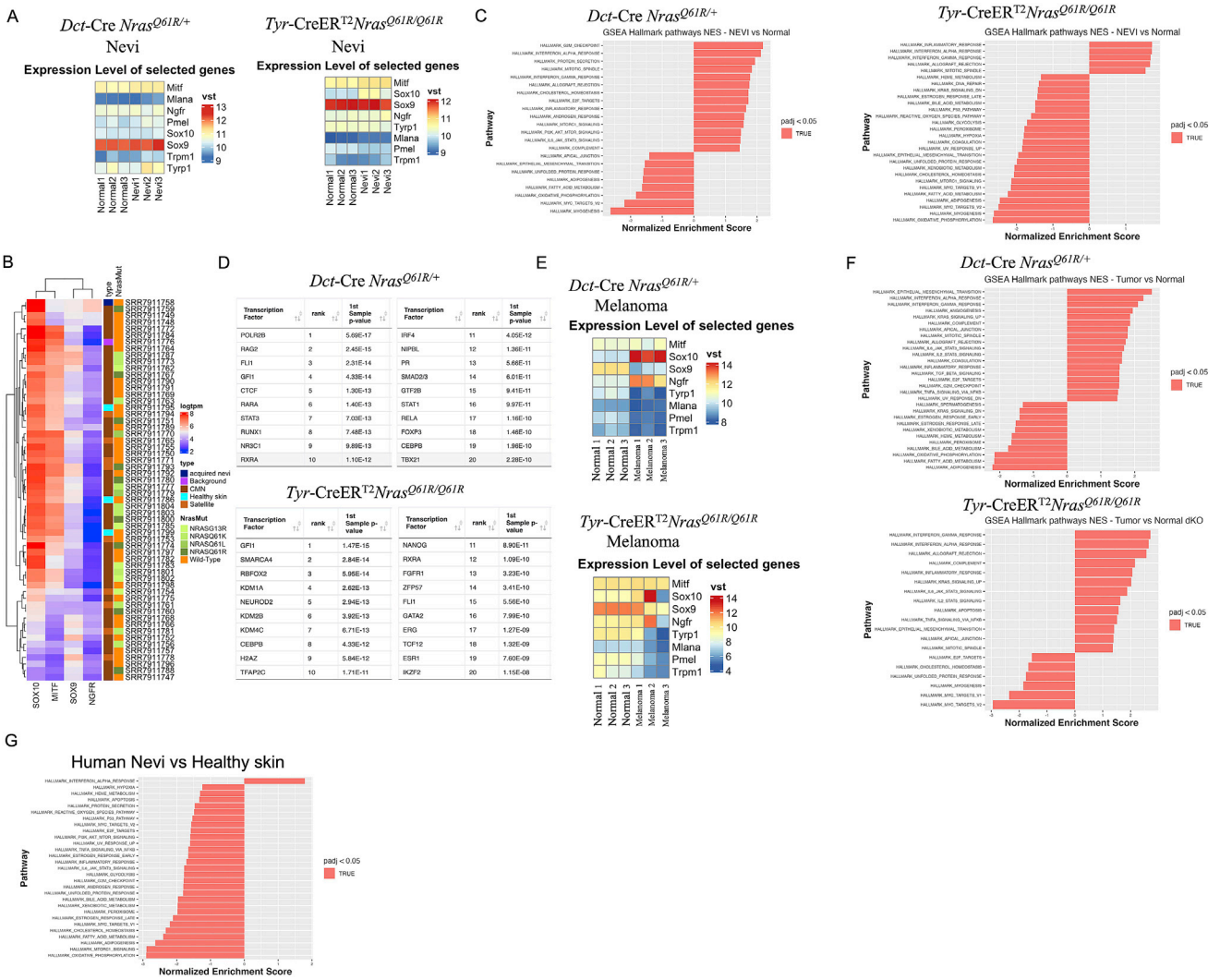

Figure S4. RNA sequencing of mouse nevi and melanoma compared with normal mouse skin and human CMN, related to Figure 3

(A) Heatmap of melanocytic genes in nevi *Nras* mouse models.

(B) Heatmap of melanocytic genes in human CMN samples.

(C) GSEA hallmark pathway analysis of nevi from *Nras* mouse models in comparison with normal skin.

(D) Top 20 LISA-predicted transcription factors based on top 200 significantly upregulated genes from the nevi vs normal skin comparison.

(E) Heatmap of melanocytic genes in melanoma *Nras* mouse models.

(F) GSEA hallmark pathway analysis of melanoma from *Nras* mouse models in comparison with normal skin.

(G) GSEA hallmark pathway analysis of human CMN samples in comparison with human healthy skin samples from the same cohort.

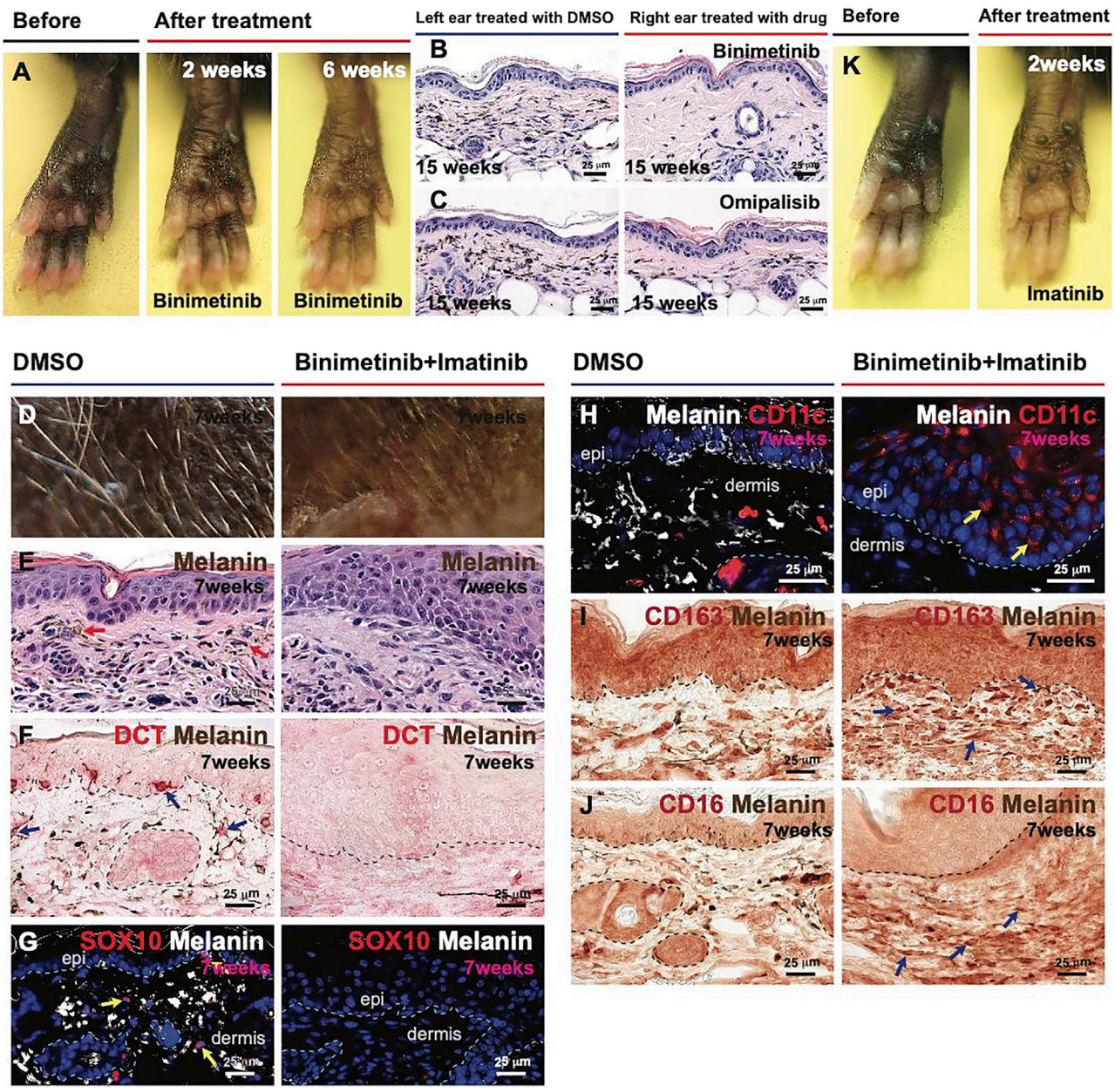

Figure S5. Kinase inhibitor treatments to induce nevus regression, related to Figure 4

(A and K) The MEK inhibitor, binimetinib (A, 0.6 μg/μL), or the c-KIT inhibitor, imatinib (K, 10 μg/μL), was subcutaneously injected into the pigmented paws of tamoxifen-induced *Tyr*-CreER^{T2} *Nras*$^{Q61R/Q61R}$ mice in 10 μL of 10% DMSO three times per week for 2 weeks. Depigmentation was then assessed 2 weeks (A and K) and 6 weeks (A) after the final drug treatment.

(B and C) Pigmented right ears of tamoxifen-induced *Tyr*-CreER^{T2} *Nras*^{Q61R} mutant mice were topically treated with the MEK inhibitor, binimetinib (B, 10 μg/μL) or the PI3K inhibitor, omipalisib (C, 10 μg/μL), five times per week for 2 months; the vehicle control, DMSO, was applied at the same time points to the pigmented left ear of the same mouse. All agents were administered topically in 5 μl DMSO. Ear skin tissues were harvested 15 weeks after the final drug treatment, and nevus regression was assessed. Melanin detected by bright-field microscopy is shown (B and C, black). Five mice per each treatment group were used, and representative images are shown.

(D–J) Topical combinatorial therapy with binimetinib (5 μg/μL) plus imatinib (50 μg/μL) was applied to the pigmented ears of tamoxifen-induced *Tyr*-CreER^{T2} *Nras*$^{Q61R/Q61R}$ mutant mice. Topical agents were administered in 5 μL DMSO, four times per week for 7 weeks. Shortly thereafter ear skin tissues were collected and analyzed. Photographic images of ear tissues are shown (D). Melanin is shown in images of hematoxylin and eosin (H&E) stained ear skin (E, brown). Red arrows in (E) indicate dermal melanin detected by bright-field microscopy. Ear skin sections were stained with DCT (F, red), SOX10 (G, red), CD11c (H, red), CD163 (I, red), or CD16 (J, red) antibodies. Blue arrows in (F), (I), and (J) and yellow arrows in (G) and (H) indicate positive signals. Melanin detected by bright-field microscopy is shown as dark brown in (F), (I), and (J) and white in (G) and (H). We used five mice per treatment group, and representative images are shown.

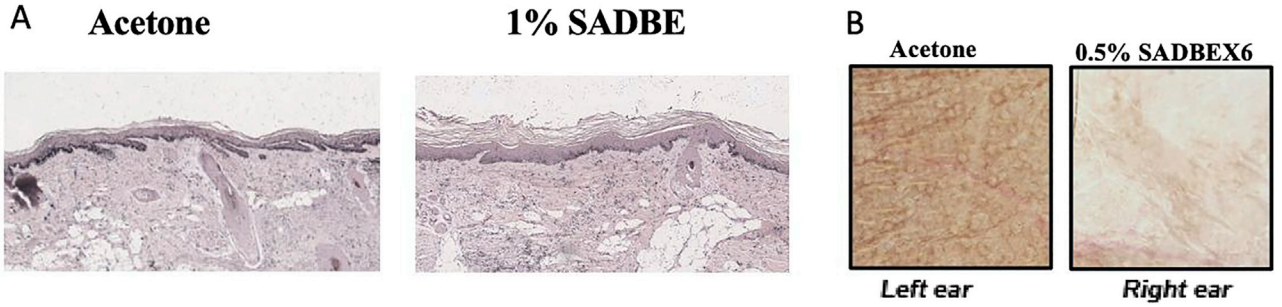

Figure S6. Fontana Masson of xenografts and efficacy of low dose SADBE in mice, related to Figure 7

(A) Fontana-Masson staining of human xenografts treated with SADBE (1%) compared with acetone control.

(B) SADBE (0.5%, topical) was applied to the pigmented right ears of tamoxifen-induced *Dct*-Cre *Nras*$^{Q61R/+}$ mutant 3 times a week for 2 weeks, and the pigmented left ears of the same animals were treated with acetone vehicle. Ear tissue images were obtained with a stereomicroscope, and dark brown particles indicate melanin.